



## Three-dimensional crustal structure of the Mariana island arc from seismic tomography

Andrew J. Calvert,<sup>1</sup> Simon L. Klemperer,<sup>2</sup> Narumi Takahashi,<sup>3</sup> and Bryan C. Kerr<sup>2</sup>

Received 17 January 2007; revised 6 October 2007; accepted 18 October 2007; published 26 January 2008.

[1] A three-dimensional (3-D) seismic refraction survey was acquired over the Mariana volcanic arc at 14.5–18.5°N and 145–147°E. First-arrival traveltimes from this survey and from a separate 2-D survey acquired approximately perpendicular to the arc have been simultaneously inverted for a 3-D  $P$  wave velocity model using seismic tomography subject to smoothness constraints. The active arc, which initiated only 3–4 Ma ago, has an average crustal thickness of 18 km. Approximately 40 km to the east the inactive remnant of the rifted Eocene arc has an average crustal thickness of 21 km, due primarily to a thicker lower-crustal layer with velocities of 6.5–7.0 km s<sup>-1</sup>. Crustal production clearly varies both temporally and spatially, with some crustal layers, including the igneous fore-arc crust, varying in thickness by a factor of up to 2 along strike. Average  $P$  wave velocities within the upper crust of the modern arc are 240–360 m s<sup>-1</sup> lower than in the Eocene arc but are 280 m s<sup>-1</sup> higher within the lower crust. Middle crust with velocities of 6.0–6.5 km s<sup>-1</sup> is best developed beneath the Eocene arc. These results suggest an evolution of arc structure with increasing age: We infer closure of fractures and porosity in the upper crust through hydrothermal circulation and a reduction in the mafic character of the middle to lower crust as a result of intracrustal differentiation. Although tonalitic rocks may predominate in the transition from upper to middle crust, the bulk of the crust is essentially basaltic.

**Citation:** Calvert, A. J., S. L. Klemperer, N. Takahashi, and B. C. Kerr (2008), Three-dimensional crustal structure of the Mariana island arc from seismic tomography, *J. Geophys. Res.*, 113, B01406, doi:10.1029/2007JB004939.

### 1. Introduction

[2] The accretion of magmatic arcs is considered to be a primary mechanism by which the continents have grown over most of Earth's history [Hamilton, 1981; Card, 1990], although tectonic processes such as accretionary wedge development, obduction of oceanic crust, and basaltic underplating also contribute. Seismic velocity measurements [Christensen and Mooney, 1995] and geochemical constraints [Taylor and McLennan, 1995] suggest that the continental crust is largely intermediate in composition, but geological and seismic observations from intraoceanic subduction zones indicate that island arc crust is commonly basaltic [Arculus, 1981; Grow, 1973; Holbrook et al., 1999]. If mafic island arcs have been common through much of Earth's history, then it is necessary to invoke processes such as magmatic reworking and lower-crustal delamination during growth [Behn et al., 2007], accretion, or shortly thereafter to explain the present-day composition of the continents [e.g., Kay and Kay, 1993]. Tonalitic rocks,

however, have been exhumed in the Izu collision zone of Japan [Nitsuma, 1989; Kawate and Arima, 1998], and a midcrustal layer of intermediate composition has been inferred in the Izu-Bonin and Tonga arcs from seismic refraction surveys [Suyehiro et al., 1996; Takahashi et al., 1998; Crawford et al., 2003; Kodaira et al., 2007]. If rocks of intermediate composition comprise a large volume of oceanic island arcs, then the present-day composition of the continental crust may be compatible with the direct accretion of island arcs to continental margins, during which most of the incoming crust is preserved [Taira et al., 1998].

[3] Wide-angle seismic surveys provide an effective way of inferring bulk crustal composition from the well-known variations of seismic velocity with mineralogy, pressure, and temperature. Although convergent continental margins have been intensively studied over the last 40 years, the number of seismic surveys of oceanic volcanic arcs is quite small [Leat and Larter, 2003]. (Some island arcs such as Japan were originally constructed on rifted continental fragments [Murauchi, 1972], and so they cannot be considered representative of the processes occurring at a true intraoceanic subduction zone.) In a two-dimensional (2-D) seismic refraction line across the Izu arc, Suyehiro et al. [1996] inferred that the arc crust was approximately 21 km thick and comprised a 6-km-thick upper crustal layer, a 6-km-thick layer with  $P$  wave velocities between 6.1 km s<sup>-1</sup> and 6.2 km s<sup>-1</sup>, that is, a layer of intermediate composition, and a 10-km-thick mafic lower-crustal layer with seismic

<sup>1</sup>Department of Earth Sciences, Simon Fraser University, Burnaby, British Columbia, Canada.

<sup>2</sup>Department of Geophysics, Stanford University, Stanford, California, USA.

<sup>3</sup>Japan Agency for Marine-Earth Science and Technology, Yokohama, Japan.

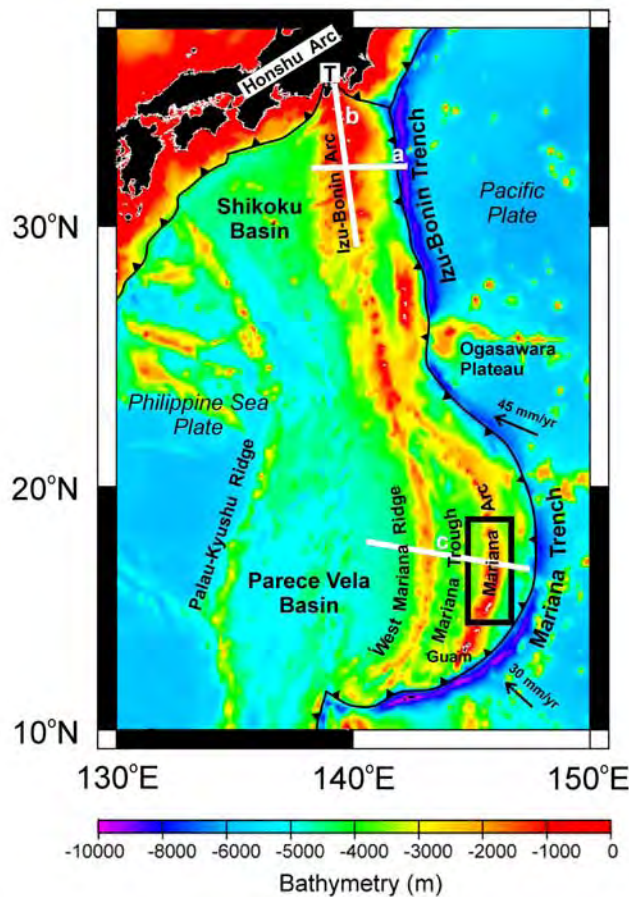


**Figure 1.** Map of NW Pacific Ocean showing the Izu-Bonin (Ogasawara)-Mariana subduction zone and associated back-arc basins. White lines indicate seismic profiles (a) across the northern Izu-Bonin arc [Suyehiro *et al.*, 1996], (b) along the northern Izu-Bonin arc [Kodaira *et al.*, 2007], and (c) across the Mariana arc-back-arc system [Takahashi *et al.*, 2007]. The relative motions between the Philippine Sea plate and the Pacific plate at the trench are marked [Seno *et al.*, 1993]. The three-dimensional (3-D) wide-angle seismic survey (Figure 2) is located within the black rectangle. T designates the exhumed Tanzawa plutonic complex in the collision zone between the Izu and Honshu arcs.

velocities from  $6.8 \text{ km s}^{-1}$  to  $7.3 \text{ km s}^{-1}$ . A subsequent survey along the Izu arc showed that the thickness of the middle-crustal layer varied between 4 km and 16 km [Kodaira *et al.*, 2007]. A 3-D analysis of a swath 2-D survey along the oceanic part of the Aleutian volcanic arc revealed a 30–37-km-thick crust, no significant thickness of intermediate composition, and  $P$  wave velocities above  $6.5 \text{ km s}^{-1}$  throughout most of the igneous crust [Holbrook *et al.*, 1999; Flidner and Klemperer, 1999, 2000; Lizarralde *et al.*, 2002; Shillington *et al.*, 2004]. Most recently, a 2-D wide-angle survey across the Mariana oceanic arc indicates that the crust here is 20 km thick with a 3–6-km-thick layer of intermediate composition possessing velocities of  $6.0$ – $6.5 \text{ km s}^{-1}$  and a 6–8-km-thick basaltic lower crust with velocities of  $6.6$ – $7.4 \text{ km s}^{-1}$  [Takahashi *et al.*, 2007].

These different results suggest that there are significant variations in the composition and evolution of ocean island arcs. Since such subsurface variability may well exist along an arc as well as perpendicular to the arc, estimates of the seismic velocity structure are desirable within as large a subsurface volume as possible. Three-dimensional wide-angle seismic surveys, which employ a large grid of shot and receiver lines, are able to image more of the subsurface than is possible with 2-D surveys and are better able to characterize the variation in seismic velocity within complex regions such as volcanic arcs.

[4] The Izu-Bonin (Ogasawara)-Mariana (IBM) volcanic arc in the northwest Pacific Ocean is a classic example of an ocean island arc system where subduction zone magmatism can be studied with minimal contamination from preexisting continental crust. Between February and April 2002, a set of regional 2-D multichannel seismic reflection lines and a 3-D wide-angle seismic survey were acquired over the Mariana arc in the area  $14.5$ – $18.5^\circ\text{N}$  and  $145$ – $147^\circ\text{E}$ . Here we present the results of a first-arrival tomographic inversion of the 3-D wide-angle survey combined with that part of the 2-D survey of Takahashi *et al.* [2007] that lay within approximately 100 km of the arc.

## 2. Tectonic Setting

[5] The IBM subduction zone, along which Late Cretaceous to Early Jurassic ocean crust of the Pacific plate descends beneath the Philippine Sea plate, extends 2800 km from Guam in the south to Japan in the north, where the northern end of the volcanic arc is colliding with the main Japanese island of Honshu [Stern *et al.*, 2003] (Figure 1). The convergence between these two plates varies between  $2.4 \text{ cm a}^{-1}$  to the WNW at  $12^\circ\text{N}$  and  $6.1 \text{ cm a}^{-1}$  to the NW at  $34^\circ\text{N}$  [Seno *et al.*, 1993]. A well-developed back-arc spreading center exists west of the Mariana segment of the subduction zone and estimates of the full spreading rate vary between  $3.0 \text{ cm a}^{-1}$  and  $4.3 \text{ cm a}^{-1}$  [Bibee *et al.*, 1980; Hussong and Uyeda, 1981], implying that the convergence rate across the Mariana Trench is approximately  $6$ – $7 \text{ cm a}^{-1}$ . The strongly arcuate geometry of the Mariana segment of the subduction zone, which has arisen as a result of back-arc spreading, implies oblique convergence along most of the trench with orthogonal convergence occurring only in the southern part of the Mariana arc system. The dip of the subducting Pacific plate increases rapidly, and the plate is probably vertical at depths between 200 km and 600 km. Beneath the Mariana arc the subducting slab appears to penetrate through the 670 km discontinuity and descend into the lower mantle, but farther north under the Izu-Bonin arc the slab flattens immediately above the 670 km discontinuity [van der Hilst *et al.*, 1991].

[6] The IBM subduction zone was initiated in the early Eocene ( $\sim 45 \text{ Ma}$ ) [Taylor, 1992; Stern and Bloomer, 1992], perhaps by the transformation to a trench of a fracture zone or weak line in the Pacific plate as a result of a change in the plate tectonic regime [Uyeda and Kanamori, 1979]. Early arc magmatism was characterized by boninitic magmas and very rapid crustal production rates until establishment of the modern-style island arc by the late Eocene ( $\sim 35 \text{ Ma}$ ) [Stern and Bloomer, 1992]. Rifting of this early arc and back-arc

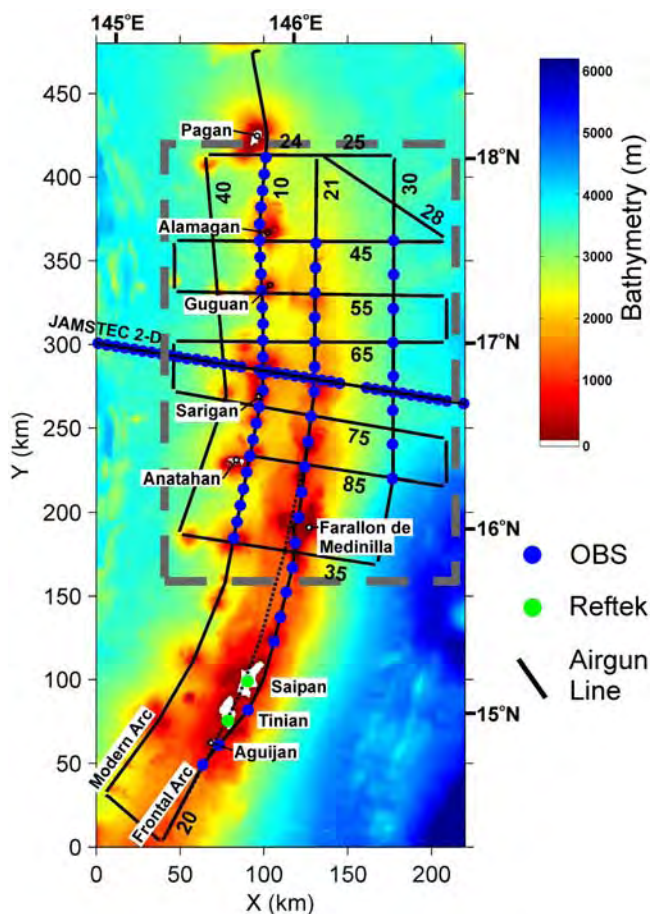


**Figure 2.** Location of the grid of airgun shot lines, 52 ocean bottom seismometers (OBS) receivers, 2 land seismometers, and the separately recorded, Japan Agency for Marine-Earth Science and Technology (JAMSTEC) 2-D OBS/airgun profile, superimposed on the bathymetry of Mariana volcanic arc at approximately  $14^{\circ}30'N$  to  $18^{\circ}30'N$  and  $145^{\circ}E$  to  $147^{\circ}E$ . Numbers of the main airgun shot lines are marked. Circular regions of shallow (<1500 m) bathymetry along line 10 correspond to the isolated volcanic centers of the modern arc. The Eocene frontal arc is the more continuous region of shallow bathymetry along line 20/21, although the seafloor depth is greater to the north. The bathymetry is a combined data set, subsampled onto a 0.5 km grid, that includes estimates from side-scan sonar and satellite altimetry and was used as a fixed seafloor interface in the tomographic inversion. The location of the primary survey grid shown in Figures 6, 7, 8, 9, and 11 is indicated by the dashed shaded box. The dashed black line indicates the location of vertical section shown in Figure 12b where it is offset from line 20/21.

spreading along most of the IBM system from 30 Ma to 15 Ma created the Shikoku basin in the north and the Parece Vela basin in the south, which separated the remnant Palau-Kyushu Ridge in the west from the still active IBM arc in the east [Hussong and Uyeda, 1981; Kobayashi et al., 1995; Okino et al., 1999] (Figure 1). The Mariana segment of the arc was subject to another rifting episode at  $\sim 8$  Ma, with seafloor spreading commencing at 3–4 Ma [Bibee et al.,

1980; Crawford et al., 1981]. Back-arc spreading in the Mariana Trough continues at the present day [Fryer, 1995], and is separating the West Mariana Ridge from the presently active Mariana arc that formed 3–4 Ma ago  $\sim 40$  km west of the remnant Eocene arc [Stern et al., 2003]. Along the Mariana segment, volcanic islands are found only in the central region, with submarine volcanoes to the north and south.

[7] The distance of the Mariana arc from continental areas has restricted the sedimentary input to the subduction zone to pelagic and volcanoclastic sediments. No significant accretionary wedge has developed because most of the incoming sediment is subducted and the fore arc is also subject to erosion [Clift and Vannucchi, 2004]. With relatively thin sedimentary cover the igneous fore-arc basement has been sampled by submarine dredging and drilling; boninites, arc tholeiites, and some peridotites have been recovered [Hickey and Frey, 1982; Bloomer and Hawkins, 1987; Pearce et al., 1992] and are interpreted to be associated with the initial evolution of the subduction zone during the Eocene. There is also evidence for pre-Eocene rocks, including Pacific mid-ocean ridge basalt (MORB) crust [De Bari et al., 1999] and accreted Cretaceous seamounts [Johnson et al., 1991], within the outer fore-arc crust. The fore-arc region extends from the magmatic front to the trench. The innermost part of the present Mariana fore arc comprises the eastern remnants from the successive rifting episodes that gave rise to the Palau-Kyushu and West Mariana ridges and, as such, dates back to the Eocene. This inactive “frontal arc,” of which the islands of Guam, Saipan, and Tinian are part, includes tholeiite and boninite basement rocks similar to those of the submerged outer fore arc [Reagan and Meijer, 1984; Hickey-Vargas and Reagan, 1987] and additional rhyodacite rocks [Meijer, 1983]. The present-day magmatic centers, which cannot be older than 3–4 Ma [Stern et al., 2003], lie 30–50 km west of the Eocene frontal arc.

### 3. Three-Dimensional Wide-Angle Seismic Survey

[8] The primary objective of the wide-angle seismic survey was to determine the variation in  $P$  wave velocity within a crustal volume that extends approximately 200 km along the Mariana arc and includes the present-day magmatic centers, the Eocene frontal arc, and the fore arc where no, or only very limited, past arc magmatism has occurred (Figure 1).

#### 3.1. Data Acquisition

[9] The 3-D survey comprised three approximately north–south oriented lines of receivers deployed along the strike of the three main geological objectives: modern arc, frontal arc, and fore arc (Figure 2). A total of 53 ocean bottom seismometers (OBS) were laid along these three lines by the R/V *Ewing*; each instrument package included a single vertical seismometer with 2 Hz natural frequency and an external hydrophone. Fifty-two of 53 OBSs yielded useful data. The receiver spacing was 10 km, 15 km, and 20 km along the modern arc, the frontal arc, and the fore arc, respectively. These OBS instruments were augmented by six three-component Reftek recorders with 4.5 Hz

natural frequency (provided by the Program for Array Seismic Studies of the Lithosphere) that were deployed on the volcanic islands, but only two instruments from Tinian and Saipan yielded useful data. After deploying the OBS instruments, the R/V *Ewing* shot four north–south lines and seven east–west lines plus six short-transit lines using a 20-gun airgun array with a total volume of 177 L (10,810 in<sup>3</sup>) fired every 200–250 m for a total of approximately 12,560 shots. All airgun lines were also recorded by a 6 km hydrophone streamer to provide low-fold reflection data to delineate the upper crust along the wide-angle profiles [e.g., Günther *et al.*, 2006]. Since each receiver recorded every shot line, seismic arrivals are available from a wide range of azimuths and offsets. The 11 primary airgun lines generated a total of 594 receiver gathers, of which only 69, or 12%, represent inline recording. Thus the bulk of the data recorded in the 3-D survey are fan profiles. The survey layout provided almost continuous ray coverage within the primary survey grid (defined in Figure 2 by 70 km (line 40)  $< x < 170$  km (line 30) and 170 km (line 35)  $< y < 420$  km (line 24/25) at depths of 10–20 km. At shallower depths, subsurface coverage becomes restricted to the vicinity of the shot and receiver lines. At depths greater than 20 km the subsurface coverage, which in practice is additionally affected by the ability to identify seismic arrivals at long offsets, decreases with increasing depth and is confined to the central part of the primary survey grid.

### 3.2. Data Quality and First-Arrival Picking

[10] In general, the recorded seismic data are of good quality after band-pass filtering 5–20 Hz. The seismic wavefield is well defined at source-receiver offsets up to approximately 80–100 km (Figure 3 and Auxiliary Material<sup>1</sup>), and first arrivals are intermittently observed at offsets greater than 120 km. In many cases the rugged topography along the shot lines defocuses the seismic energy, creating shadow zones or weaker arrivals that result in a discontinuous identification of first arrivals at far offsets. First-arrival traveltimes were readily determined at small offsets, but there was greater uncertainty in the identification of the first-arriving phase at distant offsets, making a cycle skip possible. To allow for these uncertainties, offset-dependent picking errors were assigned to the entire data set of traveltimes. These picking errors were linearly interpolated between the following source-receiver offsets: 0.05 s at 0 km, 0.05 s at 20 km, 0.1 s at 50 km, 0.15 s at 100 km, and 0.3 s at 200 km. Approximately 248,000 picks, that is, 37% of the total recovered source-receiver pairs, were made from the 3-D seismic survey. Static shifts calculated using a velocity of 3.0 km s<sup>-1</sup> were applied to the traveltimes picks from the land-based Reftek stations to correct their elevation to mean sea level.

### 3.3. JAMSTEC 2-D Survey

[11] In 2003 the Japan Agency for Marine-Earth Science and Technology (JAMSTEC) recorded a 2-D wide-angle seismic survey along an approximately east–west oriented (azimuth 099°), 700-km-long profile that extended from west of the West Mariana Ridge to the eastern Mariana fore

arc near 17°N [Takahashi *et al.*, 2003]. OBSs, which included a three-component seismometer and a hydrophone, were laid in two deployments by the R/V *Kaiyo* every 5 km over the ridges and every 10 km in the basins. Shots were fired every 200 m into the OBS using a six-gun, 194 L (12,000 in<sup>3</sup>) airgun array. The *P* wave velocity model along the entire 700 km profile is presented by Takahashi *et al.* [2007]. We have used in our 3-D traveltimes tomography approximately 30,000 first-arrival traveltimes picks from this 2-D survey where both OBS and shot lie within the area used to generate our 3-D velocity model (Figure 2).

## 4. Traveltime Inversion Methodology

[12] The nonlinear tomography problem of inverting recorded traveltimes for a 3-D subsurface velocity model can be linearized and solved iteratively. The iterative procedure requires the tracing of rays from source to receiver, which can be both time-consuming and subject to errors arising from shadow zones and multipaths. To avoid these problems, we used a tomographic inversion algorithm, first-arrival seismic tomography (FAST), based on a finite difference solution to the eikonal equation, which provides first-arrival traveltimes to all points of a 3-D subsurface velocity grid [Zelt and Barton, 1998]. Although this method provides the first arrival, this calculated phase can sometimes have very low amplitude, especially in areas of large velocity variation, and may not always correspond to the traveltimes pick. As mentioned in section 3.2, larger magnitudes were assigned to the picking errors to allow for this issue. Raypaths from each receiver back to the source are generated by following the steepest descent direction through the computed 3-D traveltimes field; this approach produces first-arrival raypaths irrespective of wave type. At each iteration a perturbation to the velocity model is obtained from the difference between the calculated and observed first-arrival times. The traveltimes calculation requires a velocity model defined on a set of nodes, that is, points regularly spaced in all three dimensions; however, the inversion step uses cubic cells from which the derivatives of traveltimes with respect to the slowness of each model cell can be calculated. Use of closely spaced forward modeling nodes improves the accuracy of the traveltimes calculation, while larger inversion cells help to reduce the large memory and computer time requirements for this latter step.

### 4.1. Initial Model

[13] An initial velocity model is required for the iterative inversion, and a simple 1-D velocity function below laterally varying seafloor and basement interfaces was used. The dimensions of the velocity model are 220 km east–west, 480 km north–south (Figure 2), and 40 km vertically. For the forward traveltimes calculation the model node spacing was 500 m, but a cell size of 1000 m was used in the inversion step. The depth to the seafloor interface varies dramatically across the survey area and, with its high seismic velocity contrast, generates highly variable time delays along the different raypaths (Figure 3). The seafloor interface gridded at a 500 m interval was obtained by subsampling by a factor of approximately 2 a bathymetric data set in which side-scan sonar and satellite-derived

<sup>1</sup>Auxiliary materials are available in the HTML. doi:10.1029/2007JB004939.

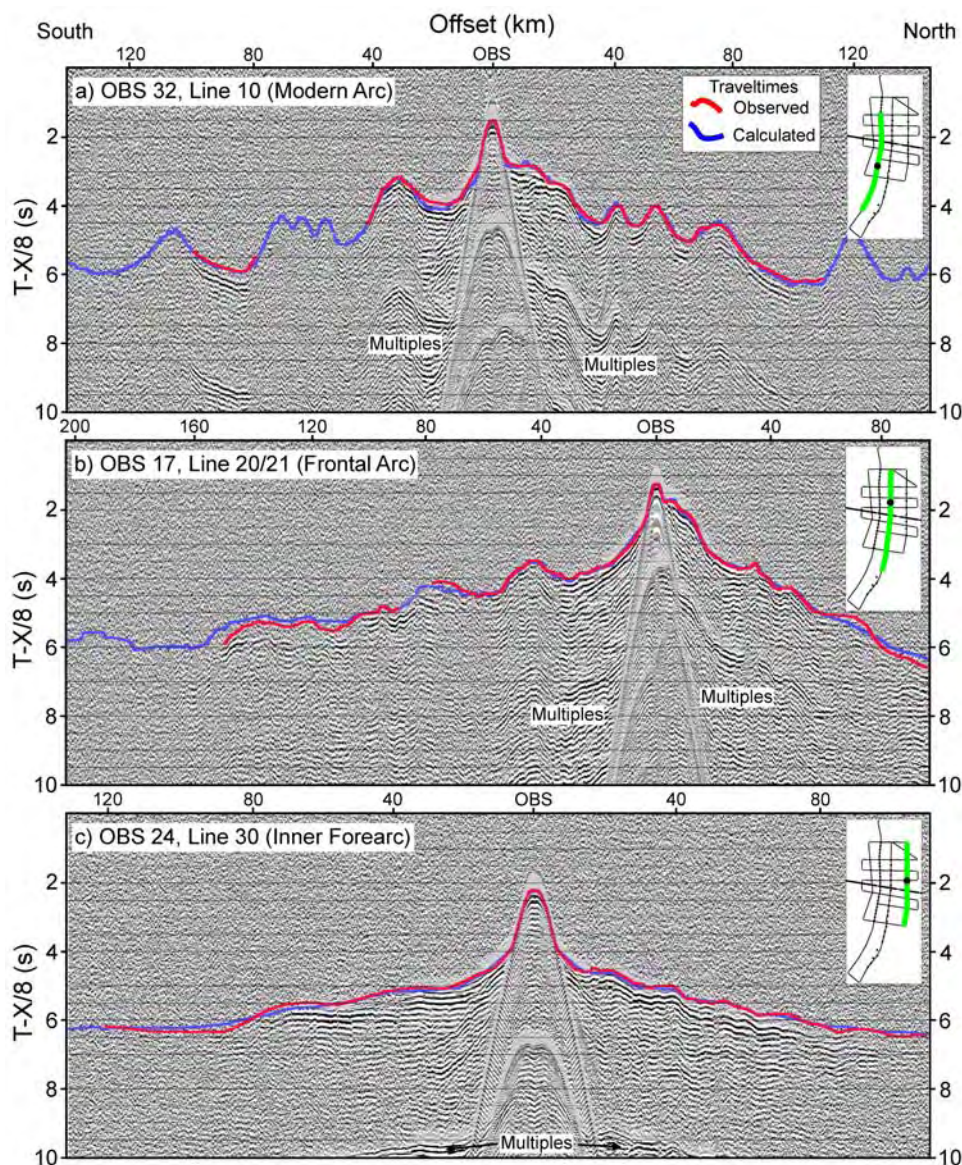


**Figure 3.** Examples of seismic record sections recorded in the 3-D survey. The first-arrival picks are shown in red and are superimposed on the first-arrival times (which are shown in blue) calculated through the final velocity model. Where no red arrivals are visible, no first-arrival picks were made. Extreme variations in first-arrival time on line 10 are due to corresponding bathymetric variation along the modern arc (Figure 2). An automatic gain control with a 1.0 s window has been applied to the data, which are reduced at  $8 \text{ km s}^{-1}$ . (a) North–south inline along the modern arc: line 10 recorded by OBS 32. (b) North–south inline along the frontal arc: line 20/21 recorded by OBS 17. (c) North–south inline over the inner fore arc: line 30 recorded by OBS 24. (d) East–west fan profile: line 55 recorded by OBS 38. (e) East–west fan profile: line 65 recorded by OBS 38. (f) East–west fan profile: line 75 recorded by OBS 38. OBS 38 is located on the modern arc.

bathymetry were combined (Figure 2), and this 500 m grid spacing governs the accuracy of the traveltimes calculation. Both the seafloor interface and the velocity in the overlying water layer,  $1.5 \text{ km s}^{-1}$ , were fixed in the tomographic inversion.

[14] The thickness and seismic velocity of the sediment layer in the initial model were defined using the seafloor depth and constrained by estimates of the depth to the igneous basement estimated from the multichannel reflection profiles. The thickness of the sediment layer increases

linearly from zero at a water depth of 1000 m to a maximum value of 1250 m at a water depth of 2500 m, and the seismic velocity in this layer increases from  $1.5 \text{ km s}^{-1}$  at the seafloor at a gradient of  $1.0 \text{ s}^{-1}$ . This simple model represents well both the onlap of the sediment layer against the volcanic edifices and its thickness in the deep ocean basin, with the exception of the extreme west of the velocity model where the sediment layer is quite thin across the relatively young, rugged basement topography near the back-arc spreading center. The sediment layer was therefore

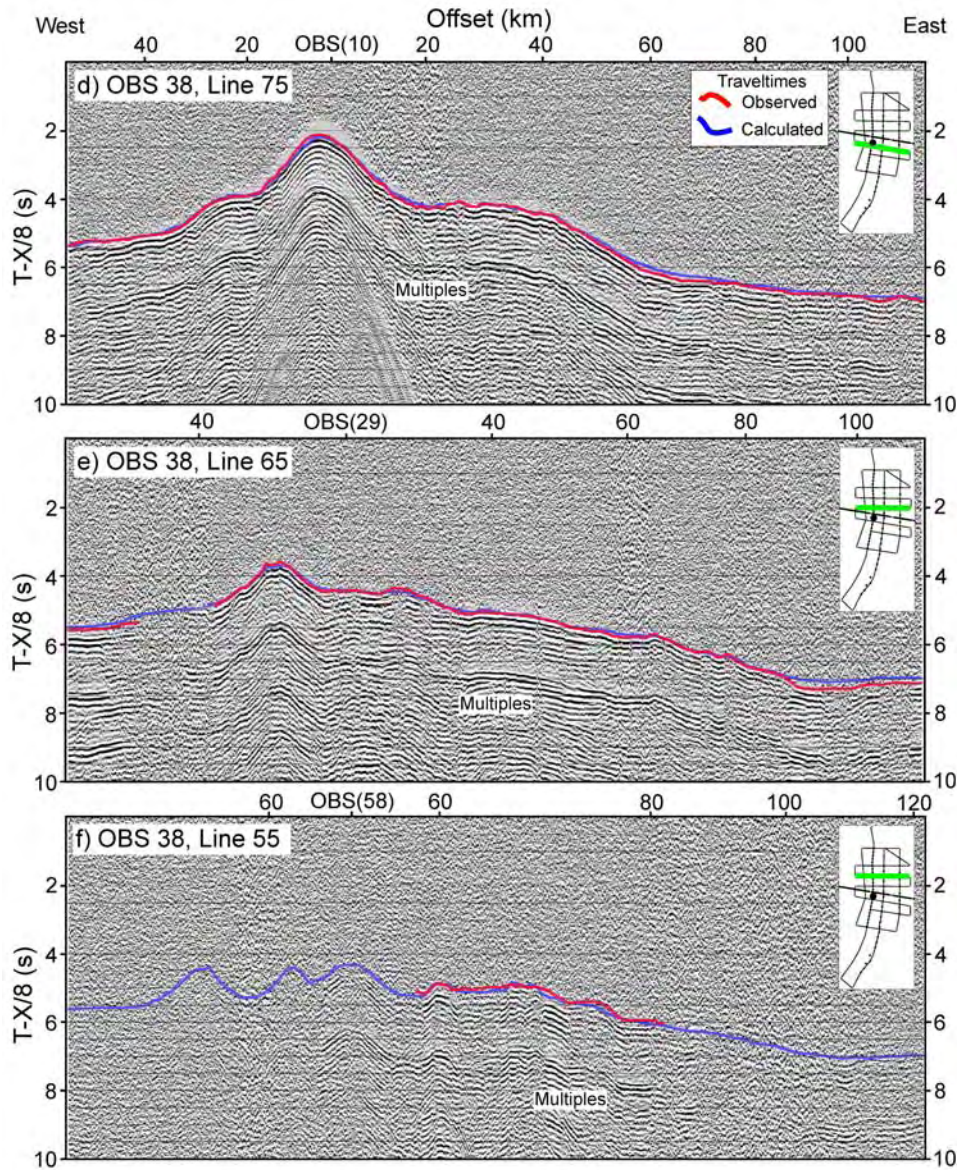


Figure 3. (continued)

set to zero in the westernmost 30 km of our initial model along the JAMSTEC 2-D line.

[15] In the initial model the velocity in the igneous crust was fixed at  $3.0 \text{ km s}^{-1}$  above 1.0 km but increased as an inverse exponential with increasing depth, asymptotically approaching a limiting velocity,  $V_M$ , of  $8.0 \text{ km s}^{-1}$  (Figure 4):

$$V_p(z) = V_M - (V_M - 3) \exp[-0.13(z - 1)].$$

[16] A variety of different initial models were tested for the iterative tomographic inversion, including representations of the igneous crust by one- and two-layer linear velocity functions; however, discontinuities in the values of the  $P$  wave velocity or its derivatives created artifacts in the final model, for example, a vertical velocity change at the depth of the initial Moho. Therefore a continuously differentiable function was chosen to represent the velocity variation in the igneous crust below a depth of 1000 m.

The shallowest velocity of  $3.0 \text{ km s}^{-1}$  in the igneous crust was constrained by the need to fit the near-offset traveltimes along the modern and frontal arcs, and  $8.0 \text{ km s}^{-1}$  was chosen as a representative starting estimate for the  $P$  wave velocity in the upper mantle. Different values of the coefficient in the exponent were tested, and the selected value gave the lowest root-mean-square (RMS) difference between the calculated traveltimes and the first-arrival picks in a simple grid search.

#### 4.2. Nonlinear Optimization

[17] Although the water layer was fixed, seismic velocities in the sediment layer, igneous crust, and upper mantle were updated during each iteration of the tomographic inversion. Regularizing constraints were based primarily on the second spatial derivatives (horizontal and vertical) of the model slownesses. Ratios of vertical to horizontal smoothness between 5% and 30% were tested, and a value

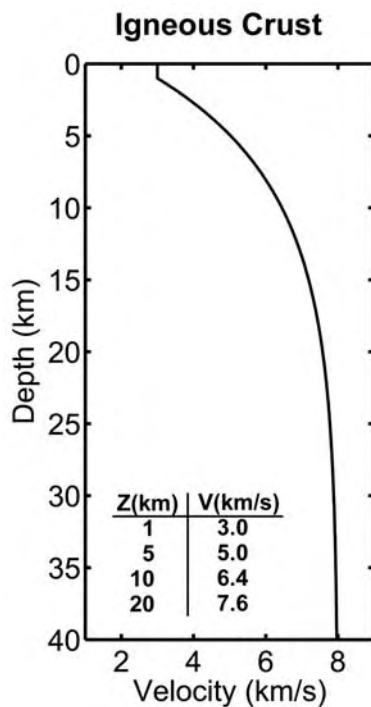


**Figure 4.** Initial 1-D  $P$  wave velocity model used in the igneous crust for the nonlinear tomographic inversion, shown with a table of velocity values at various depths in the initial model. To avoid generating artifacts in the final model, no discontinuity at the Moho interface is included.

of 20% was selected as it produced the fewest apparent artifacts (e.g., strong decreases of velocity with depth or velocity perturbations concentrated on regions of high ray density) in intermediate and final velocity models. A constraint on the difference between the model update and the initial model was also applied, but this was weighted at only 1% of the smoothness constraints. During each nonlinear iteration, three values of the tradeoff parameter between the model constraints and traveltime misfit were tested, but this parameter was reduced by a factor of at most 2 between iterations. Limiting the decrease in the tradeoff parameter slowed the convergence of the tomographic inversion, necessitating more iterations, but this approach resulted in the desired development of mostly long wavelength structures during early iterations. (For further details, see Zelt and Barton [1998], Ramachandran [2001], and Ramachandran *et al.* [2004].) Nine iterations were computed, which reduced the RMS traveltime residual from 0.420 s to 0.119 s, corresponding to a reduction in the normalized  $\chi^2$  value from 17.0 to 1.0.

[18] The value of the RMS traveltime residual for the entire 3-D survey gives no indication of the existence of large residuals in certain parts of the traveltime data. Therefore the traveltime residuals for all shot azimuths into each receiver were binned by offset and displayed (Figure 5). Detailed examination of these residuals indicates that the majority of observed traveltimes are reproduced well by the final velocity model and that most errors are associated with offsets greater than 120 km. To determine whether these larger residuals at far offsets significantly

affect the final model, we recomputed the tomographic inversion with only source-receiver offsets less than 120 km. The mean difference in velocity magnitude between the two models computed on a cell-by-cell basis is  $<0.5\%$  above a depth of 27 km, which we do not consider significant, but there are differences in the maximum depth of ray coverage in the center of the velocity model.

#### 4.3. Model Assessment

[19] The regions of the final 3-D velocity model constrained by the wide-angle seismic survey are related to the geometry of subsurface ray coverage, which is greater than 100 rays per 1 km cubic cell along the north-south receiver lines at depths shallower than 15 km and along the east-west JAMSTEC 2-D line at depths less than 22.5 km (Figure 6). Although some small gaps in ray coverage exist at depths between 10 km and 22.5 km, the velocity model is considered to be reasonably well constrained over this depth range because of the continuity and extent of the ray coverage.

[20] To assess the lateral resolution of the final velocity model, a series of 2-D checkerboard tests with horizontal grid dimensions (half wavelengths) of 10 km, 20 km, 30 km, and 40 km were performed using the same model constraints, grid/cell dimensions, and source-receiver configuration as the original tomographic inversion [e.g., Zelt, 1998]. The model, with the exception of the fixed water layer, was subject to a laterally varying sinusoidal perturbation of given half wavelength; the maximum value of the perturbation was 10% of the velocities of the final model. Traveltimes were calculated for this perturbed model, and Gaussian noise with the same standard deviation as the original picks was added. These traveltimes were then inverted using the nonperturbed velocity values as a starting model. The degree to which these lateral velocity perturbations can be recovered provides an indication of the degree of lateral resolution in the final velocity model as a function of depth. The ideal result of such a test is vertically oriented sinusoidal banding that extends uniformly across the velocity model below the seafloor and appears as a 2-D sinusoid in horizontal slices through the 3-D model. The 40 km checkerboard is well recovered above 17.5–20 km depth and is partially recovered at depths as great as 25 km in the eastern half of the primary survey grid defined in section 3.1 (Figure 7a). The 30 km checkerboard (not shown) is well recovered in the main survey grid above 15 km depth, except for the extreme NW and SE corners, and is partially recovered at depths as great as 20 km in the eastern half of the main survey. The 20 km checkerboard is well recovered above 12.5–15 km depth within the main survey grid, with the exception of the extreme SE corner (Figure 7b). The 10 km checkerboard is not well recovered anywhere within the velocity model and is not shown.

[21] To assess the vertical resolution of the velocity model, we computed 3-D checkerboard tests in which the sinusoidal perturbation had half wavelengths of 5 km and 10 km in the vertical direction and 30 km in both the horizontal dimensions. The sinusoidal perturbation with 10% peak amplitude was imposed on the final model at depths greater than 2 km below the seafloor to avoid large changes to raypaths close to the sources and receivers. The 10-km-thick anomalies are recovered at depths above 20 km

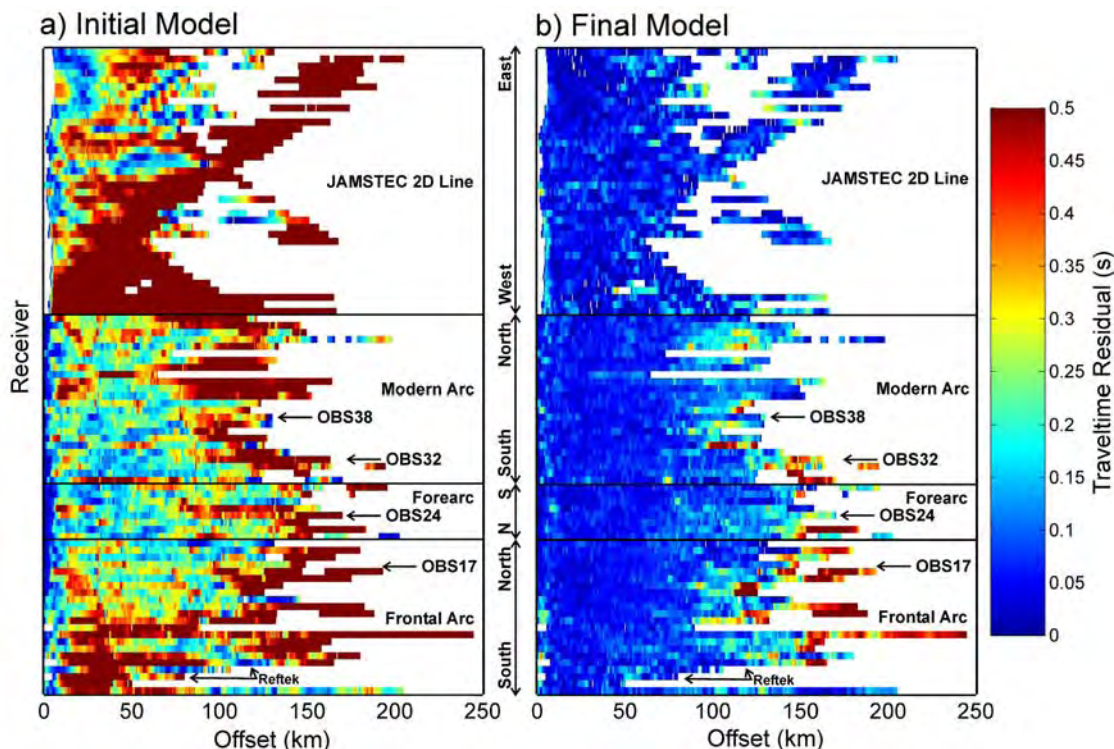


**Figure 5.** Multi-azimuth traveltimes residuals for each receiver binned by source-receiver offset for (a) initial model and (b) final model. Traveltime residuals between the first-arrival picks and times calculated through the two velocity models were binned by source-receiver offset at 0.5 km intervals. Thus each bin contains the traveltime residual averaged over the range of recorded azimuths. For the final velocity model, traveltime residuals are less than 0.1 s at most offsets less than 120 km; however, residuals are greater than 0.2 s for a number of receivers deployed along the frontal arc at offsets greater than 150 km.

across most of the primary survey grid, but the rectangular shape is more distorted near 20 km depth and approaching the edges of the main survey area (Figure 8a). Anomalies are sometimes detectable at depths below 20 km, but their shape is poorly resolved. The 5-km-thick anomalies are best resolved at depths between 5 km and 15 km (Figure 8b). Between 15 km and 20 km depth, positive velocity anomalies are commonly resolved, but the identification of negative anomalies is problematic because of the decrease in spatial resolution with increasing depth characteristic of crustal-scale refraction surveys.

### 5. Three-Dimensional Velocity Model

[22] The final 3-D velocity model is shown in Figure 9 with areas of zero ray coverage in the final tomographic iteration colored white. The velocity model is displayed as a series of horizontal slices at depth intervals of 2.5 km. The location of the modern active volcanic arc and the Eocene frontal arc correspond to the two longest approximately north–south lines along which airgun shots were fired. Subject to the constraints of ray coverage, it is clear that at depths less than approximately 10 km the frontal arc exhibits higher average  $P$  wave velocities than the modern arc. At a depth of 7.5 km below sea level, for example,  $P$  wave velocities along the frontal arc are almost everywhere between  $6.0 \text{ km s}^{-1}$  and  $6.5 \text{ km s}^{-1}$ ; in contrast, along the modern arc, velocities only exceed

$6.0 \text{ km s}^{-1}$  in three relatively small areas that extend 20–40 km along strike. At depths greater than 12.5 km,  $P$  wave velocities in the frontal arc are lower than the modern arc; for example, at a depth of 15 km,  $P$  wave velocities along the frontal arc are almost everywhere  $<7.0 \text{ km s}^{-1}$ , but along the modern arc velocities at the same depth are  $7.0\text{--}7.4 \text{ km s}^{-1}$ . These general observations are consistent with a thinner and more mafic crust under the modern arc than under the Eocene frontal arc, but the depth of the Moho within the 3-D velocity model must be better constrained before such an inference can be conclusively drawn.

[23] The Moho, conventionally assumed to separate crustal rocks from upper mantle rocks, and by definition separating rocks with velocities above and below  $7.6 \text{ km s}^{-1}$  [Steinhart, 1967], is not particularly well defined in the final 3-D velocity model because the tomographic inversion used only first arrivals. In velocity models generated using this approach, relatively sharp interfaces such as the Moho are commonly represented by much smoother increases in velocity that may extend over a few kilometers. We have therefore estimated the isovelocity contour in our final model that approximates the Moho by comparing the velocity model along the JAMSTEC 2-D profile, which was derived by Takahashi *et al.* [2007] using both first arrivals and wide-angle  $PmP$  reflections with a coincident vertical section extracted from our final 3-D model (Figure 10). In the JAMSTEC 2-D velocity model the

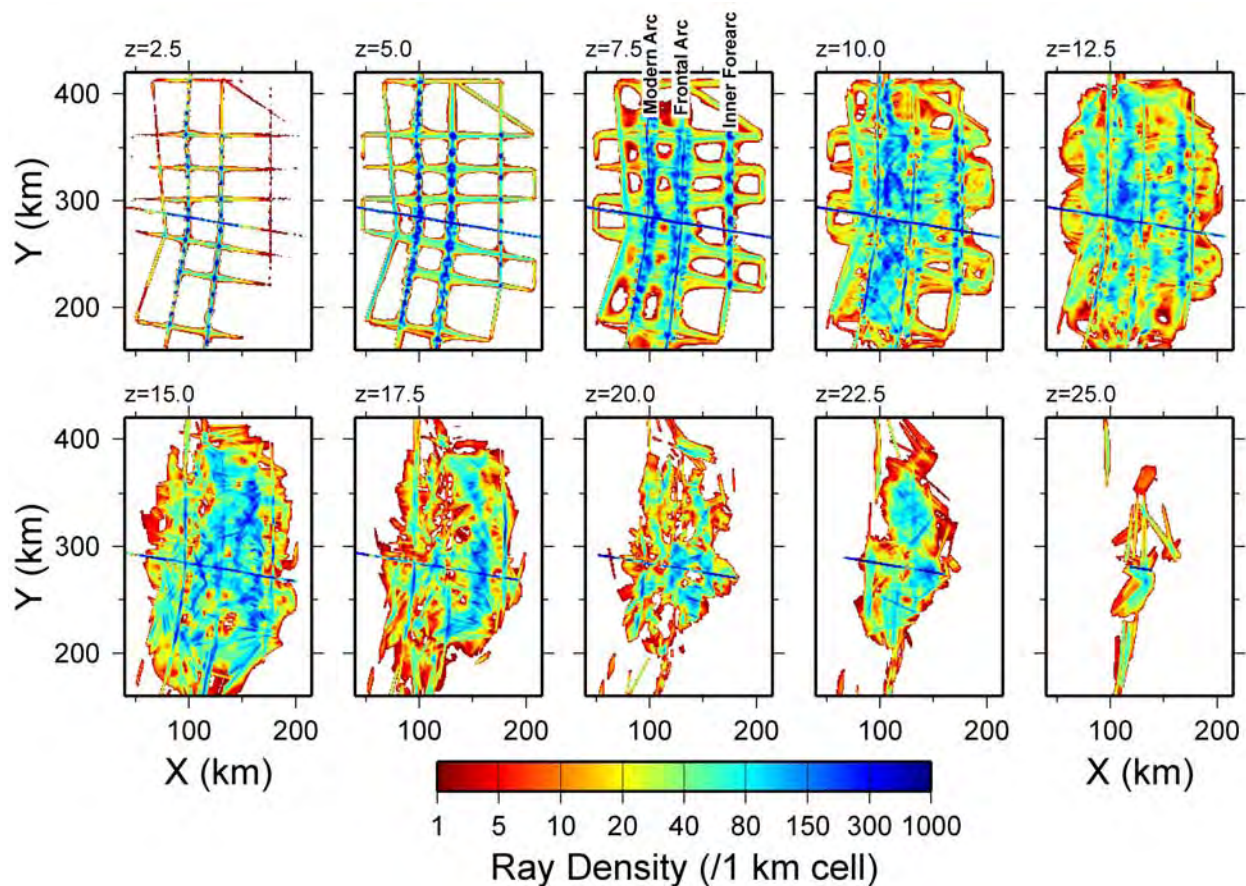


**Figure 6.** Density of ray coverage in each cubic 1 km cell at different depths within the final 3-D velocity model (thick dashed grey line in Figure 2). At depths less than 5 km, raypaths are confined to regions near the shots and receivers, but between 10 km and 20 km depth ray coverage is continuous across the primary survey grid. At depths greater than 20 km the areal coverage diminishes with increasing depth and is confined to a region close to line 20 below 25 km depth.

Moho is represented by a reflecting interface (not an isovelocity contour), across which the  $P$  wave velocity increases from  $7.3 \pm 0.1 \text{ km s}^{-1}$  to  $7.7 \pm 0.1 \text{ km s}^{-1}$  at a depth of 19–20 km beneath both modern and frontal arcs. Similarly, the “base midcrust” in Figure 10 is an interface in the model of *Takahashi et al.* [2007], across which the velocity increases from  $6.4 \pm 0.1 \text{ km s}^{-1}$  to  $6.7 \pm 0.1 \text{ km s}^{-1}$  beneath modern and frontal arcs. In the coincident section extracted from our 3-D model, there is no sharp interface at the Moho. The  $7.4 \text{ km s}^{-1}$  isovelocity contour correlates well ( $\pm 1 \text{ km}$ ) with the Moho interface at 19.5 km depth beneath the modern arc and also farther west ( $\pm 1.7 \text{ km}$ ) where the arc Moho shoals to 13.5 km outside the primary survey grid (Figure 10a). Immediately beneath the frontal arc, the  $7.4 \text{ km s}^{-1}$  contour deepens to as much as 23.5 km below sea level, some 3.5 km below the Moho interface. Farther east within the primary survey grid, whose eastern edge is defined by line 30, the contour varies from 1 km below to 2.5 km above the Moho interface. With the exception of a narrow region beneath the frontal arc the greatest discrepancies between the  $7.4 \text{ km s}^{-1}$  contour and the Moho interface inferred by *Takahashi et al.* [2007] occur in the fore-arc and back-arc regions outside the primary

survey grid, where the 3-D model is less well constrained. The JAMSTEC 2-D line intersects the frontal arc where the crustal thickness is changing along strike (Figure 11a), and the larger mismatch here may be partly attributable to the effects of out-of-plane propagation. Although we recognize that there may be localized discrepancies of up to approximately 3 km, we have used the  $7.4 \text{ km s}^{-1}$  contour as the most practical proxy for the Moho throughout our 3-D velocity model.

### 5.1. Crustal Thickness

[24] Using our 3-D velocity model, we have estimated the igneous crustal thickness within the primary survey grid where the Moho, that is, the  $7.4 \text{ km s}^{-1}$  isovelocity contour, is best constrained by the available ray coverage (Figure 11a). We consider the igneous crust to be defined by the depth interval between the  $2.9 \text{ km s}^{-1}$  and  $7.4 \text{ km s}^{-1}$  contours. Velocities of  $3.0 \text{ km s}^{-1}$  were introduced into the uppermost igneous crust in our model to reproduce the traveltimes observed at small offsets, and thus these velocities characterize most of the volcanic edifices. With a velocity bound of  $2.9 \text{ km s}^{-1}$ , however, sedimentary rocks such as carbonates, which possess relatively high velocities, may be

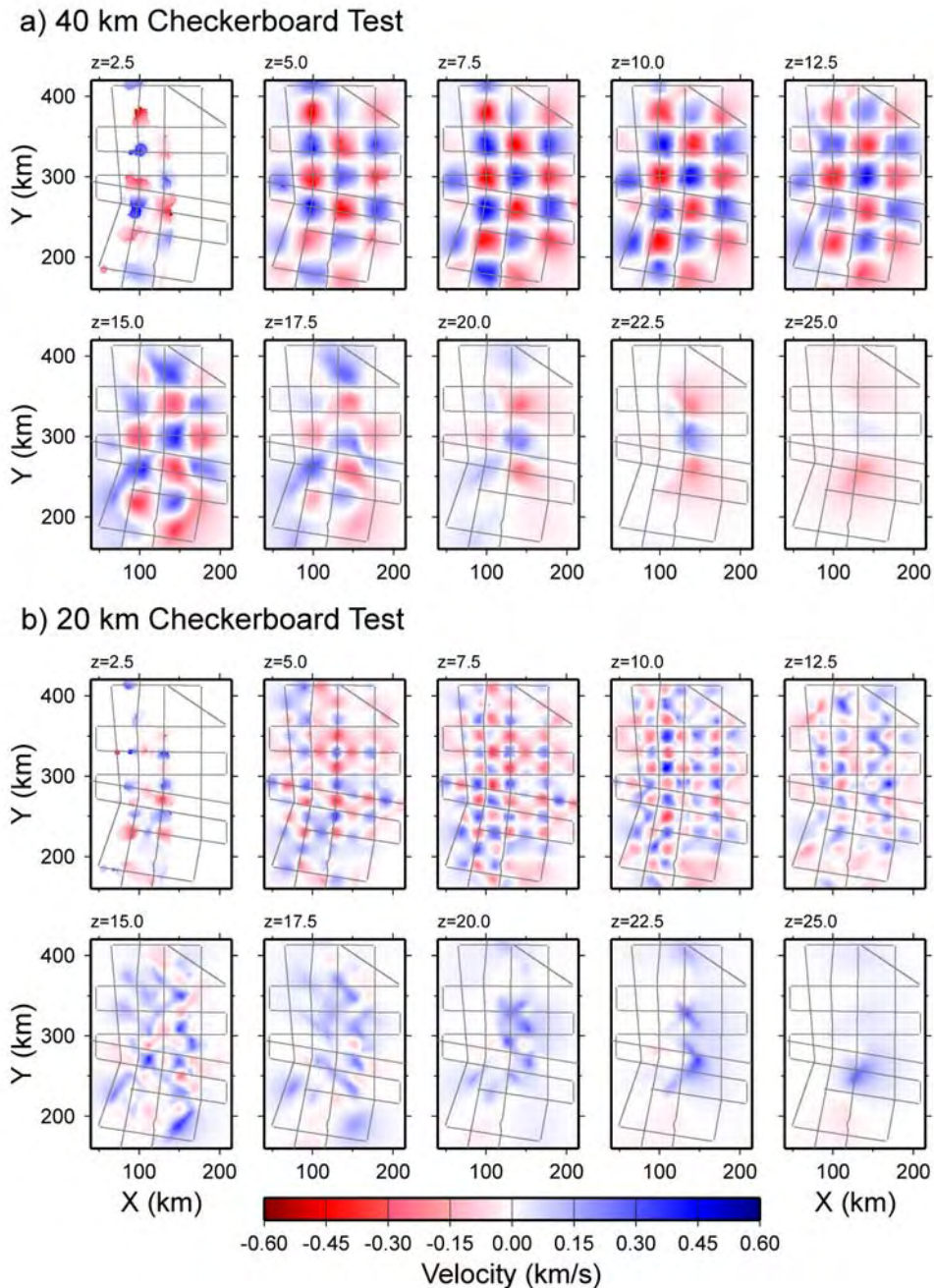


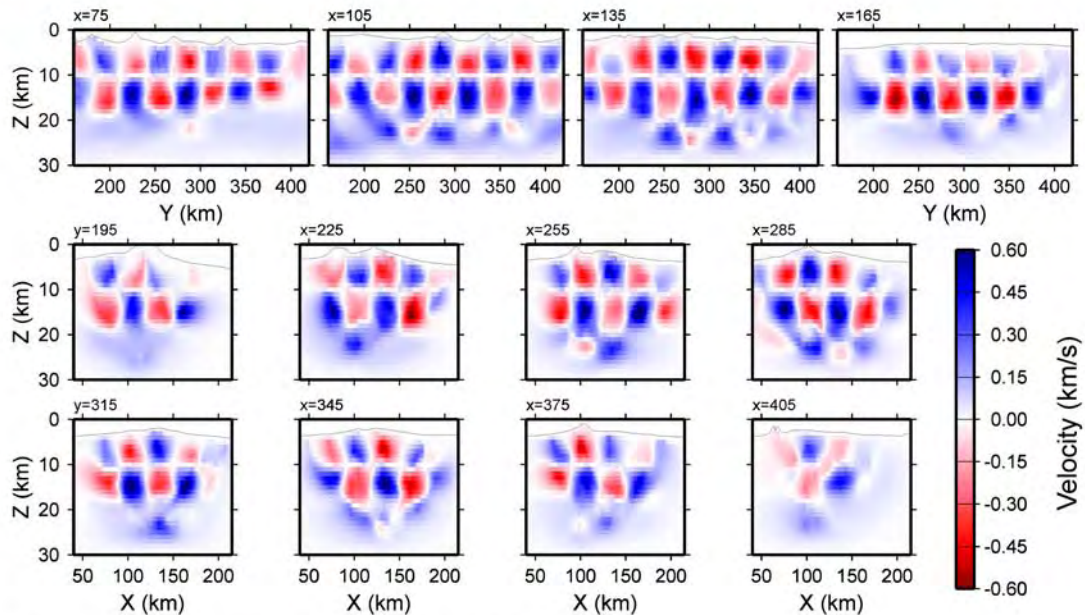
**Figure 7.** Checkerboard tests showing lateral resolution of the final 3-D velocity model at different depths for (a) 40 km  $\times$  40 km cells and (b) 20 km  $\times$  20 km cells. The 40 km checkerboard anomalies are well recovered across the main survey grid above 17.5 km depth and can still be identified at depths as great as 25 km near line 20/21. With the exception of the SE corner, the 20 km checkerboard pattern is recovered in the primary survey grid at depths less than 12.5–15 km.

included in our estimate of the igneous crustal thickness, but such contributions are likely to be small and less than the discretization of the velocity model.

[25] We have assessed the stability of our estimate of crustal thickness by using alternative initial velocity models in which the limiting upper mantle velocities at depth were  $7.6 \text{ km s}^{-1}$  and  $8.4 \text{ km s}^{-1}$ . Within the region of ray coverage the depth to the  $7.4 \text{ km s}^{-1}$  contour in the final

model varied by less than 2 km with the exception of a 30-km-long section of the frontal arc ( $295 < y < 325$ ). In these tests, however, the depth to the  $7.5 \text{ km s}^{-1}$  isovelocity contour varied by more than 4 km across a much wider area of the models, suggesting that this contour is not particularly well constrained where it lies deepest along the frontal arc. On the basis of these assessment tests, we consider our estimate of crustal thickness using the  $7.4 \text{ km s}^{-1}$  contour to

## a) 30 km x 10 km Checkerboard Test



## b) 30 km x 5 km Checkerboard Test

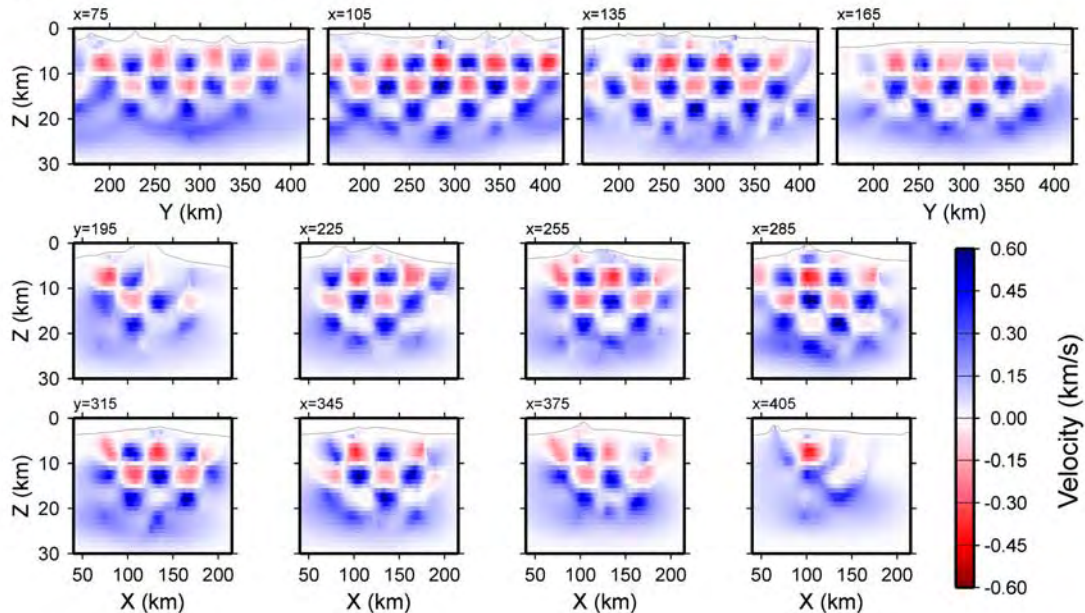


**Figure 8.** Checkerboard tests showing vertical resolution of final model along a range of north–south and east–west sections through the primary survey grid with (a) 30 km  $\times$  30 km  $\times$  10 km cells and (b) 30 km  $\times$  30 km  $\times$  5 km cells. Vertical sections have been extracted at the peaks of the horizontal sinusoidal variation. Vertical exaggeration is 5:1.

be quite reliable (approximately  $\pm 1.5$  km) along the active arc and reasonably so (approximately  $\pm 2.5$  km) along the frontal arc.

[26] The igneous crust of the frontal arc is thickest in the southern half of the main survey grid, reaching 22–24 km, and thins to 18–20 km farther north (Figure 11a). Along the modern arc the crustal thickness reaches 20 km beneath most of the volcanoes but decreases to approximately 13–16 km

between them; this variation in crustal thickness is partly due to the inclusion of the volcanic edifices in the igneous crustal estimate. To the east of the frontal arc the igneous fore-arc crust has a thickness of 13 km in the northern part of the survey grid, but the crust thins to 8 km in the south. It should, however, be noted that the correlation with the JAMSTEC 2-D profile (Figure 10a) suggests that the igneous crustal thickness could be up to 2 km greater in

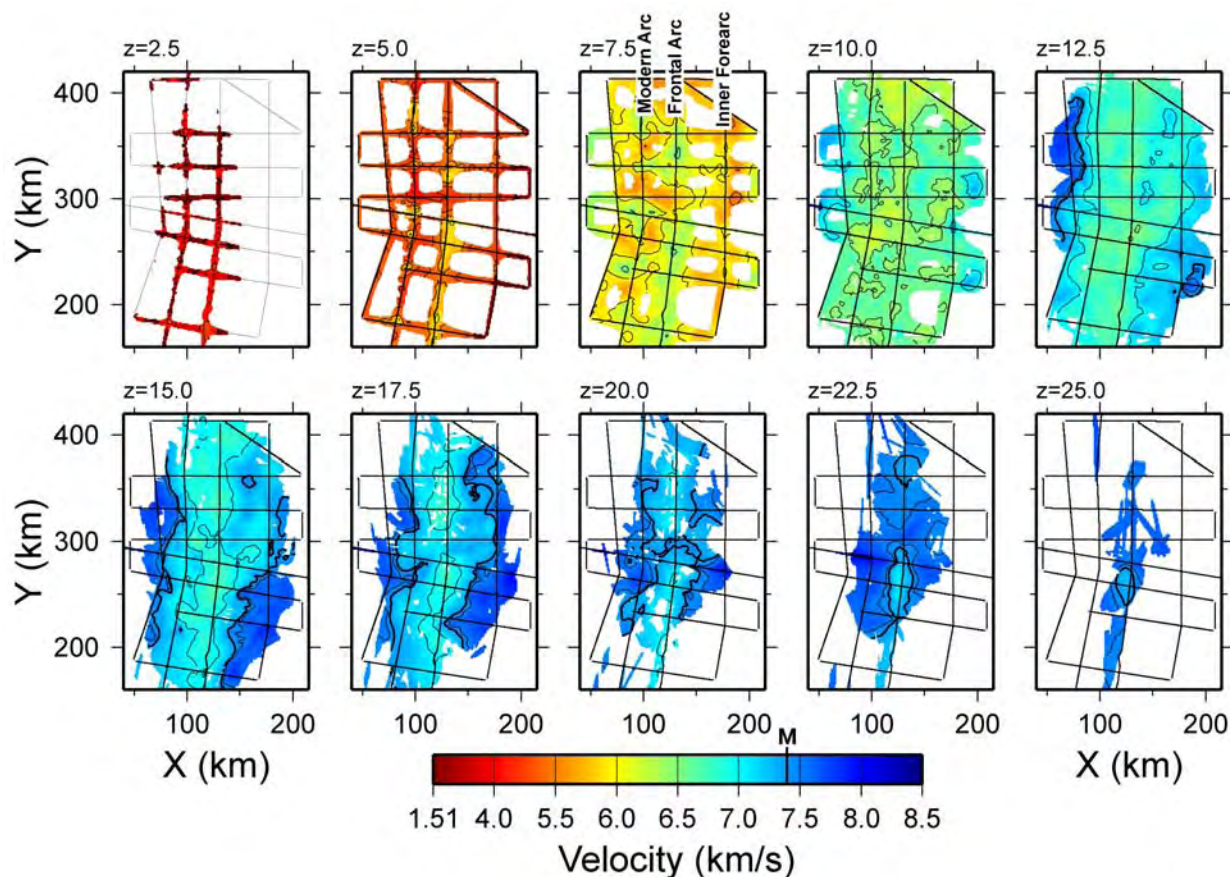


**Figure 9.** Depth slices through the final velocity model with areas of zero-ray coverage shaded white. The lines along the modern arc, Eocene frontal arc, and fore arc are labeled on the 7.5 km section. Above depths of 10 km the frontal arc possesses higher  $P$  wave velocities, but below 15 km the modern arc has higher velocities, suggesting a thinner crust. M indicates the  $7.4 \text{ km s}^{-1}$  isovelocity contour, which is shown by a thicker black line.

the fore arc than the above estimates, which are based on the  $7.4 \text{ km s}^{-1}$  isovelocity contour. To the west of the modern arc the crust thins to approximately 6 km, but, with the exception of its eastern side where OBS were deployed along line 30, changes in crustal thickness close to the edges of the survey grid are not well constrained.

## 5.2. Crustal Layer Isopachs

[27] We have calculated isopach maps of the middle and lower crust as defined by the velocity ranges  $6.0\text{--}6.5 \text{ km s}^{-1}$  and  $6.5\text{--}7.4 \text{ km s}^{-1}$ , respectively (Figures 11b and 11c). These particular velocity intervals have been selected to facilitate comparisons with previously published seismic results from other oceanic arcs. As with the crustal thickness estimate these maps are restricted to the area of the primary survey grid where the constraint by the data, which can be judged from the ray coverage of the 3-D velocity model (Figure 6), is greatest. In the 3-D model, velocities of  $6.0 \text{ km s}^{-1}$  are constrained by ray coverage up to 20 km from the shot lines, but there are gaps in coverage in the centers of some of the rectangles defined by the survey grid (Figure 11b).

[28] Disregarding structures extending less than 20 km along strike, which we consider to be the limit of resolution

of the 3-D tomographic inversion, the thickness of the midcrust varies between 2 km and 5 km along the modern arc and only reaches a significant thickness near Sarigan, where three volcanoes have merged into a larger structure. Along the frontal arc the midcrustal layer is clearly better developed, but it is not of uniform thickness along strike, varying between 3 km and 6 km. Along the modern arc the thickness of the lower crust exceeds 12 km near the volcanic centers but thins to 5–9 km between them. Although thicker along the frontal arc, the lower crust thins from 15–18 km in the southern part of the primary survey grid to 12–15 km in the north, reflecting the change in crustal thickness shown in Figure 11a. Near the modern arc many of the isovelocity contours in the middle and lower crust define approximately circular features, for example, near Alamagan, Sarigan, and Anatahan. In contrast, the contours beneath the frontal arc are subparallel to strike beneath the frontal arc.

## 5.3. Upper Mantle Velocities

[29] In general,  $P$  wave velocities in the upper mantle are not particularly well constrained across the 3-D velocity model owing to the relatively small number of travelt ime picks available at far offsets; the limited number of picks at

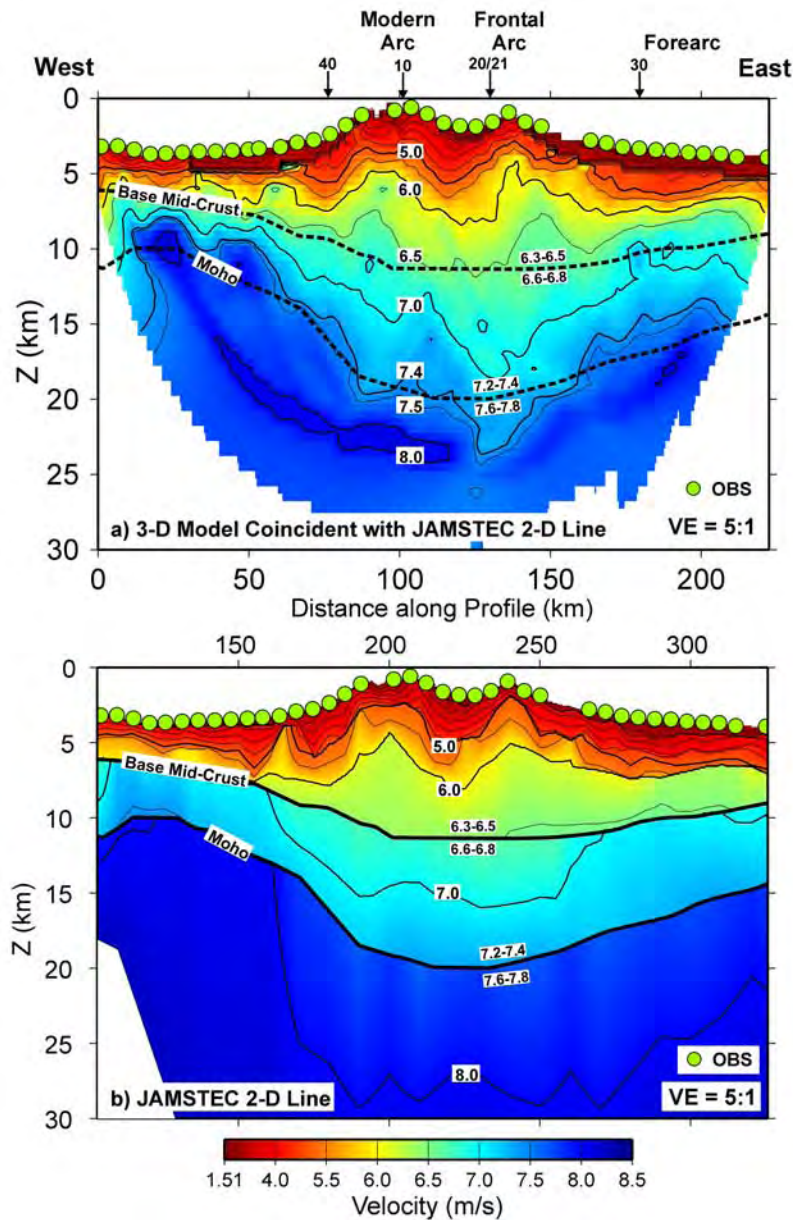


**Figure 10.** Comparison of 3-D velocity model and JAMSTEC 2-D model. (a) The vertical section was extracted from 3-D model along the JAMSTEC 2-D profile. The 3-D velocity model indicates that crustal velocities extend to greater depth beneath the frontal arc than the modern arc. The intersection points with the north–south shot lines of the 3-D survey, that is, the east–west extent of the primary survey grid, are indicated by arrows across the top of the section, and the Moho and the base of the middle crust inferred in the JAMSTEC 2-D velocity model are shown by the dashed black lines. (b) The JAMSTEC 2-D velocity model was obtained using first arrivals and wide-angle reflections. The Moho and the base of the middle crust identified using wide-angle reflections [Takahashi *et al.*, 2007] are shown by the continuous thick black lines; the velocity contrasts across these interfaces are also indicated, and the locations of JAMSTEC OBS receivers are shown by the solid green circles.

distances greater than 120 km arises from both the length of the east–west shot lines in the primary survey grid and the difficulty in detecting first arrivals at long offsets because of seismic attenuation in the arc and the background noise level. The highest velocities constrained by the 3-D survey, which are 7.7–7.8 km s<sup>-1</sup>, occur in the northwest and southwest corners of the velocity model ( $z = 12.5$  km and  $z = 17.5$  km depth slices in Figure 9, respectively) where

6–9-km-thick crust is present at the edge of the volcanic arc. Elsewhere beneath the thicker crust of the arc the velocities increase gradually with depth from 7.4 km s<sup>-1</sup>, but usually the 7.6 km s<sup>-1</sup> contour is deeper than the limit of ray coverage. The deepest ray coverage occurs beneath the long north–south shot lines over the modern and frontal arcs, where velocities of 7.6–7.7 km s<sup>-1</sup> are found (Figure 9). Beneath the JAMSTEC 2-D line, velocities of 8.0 km s<sup>-1</sup>,

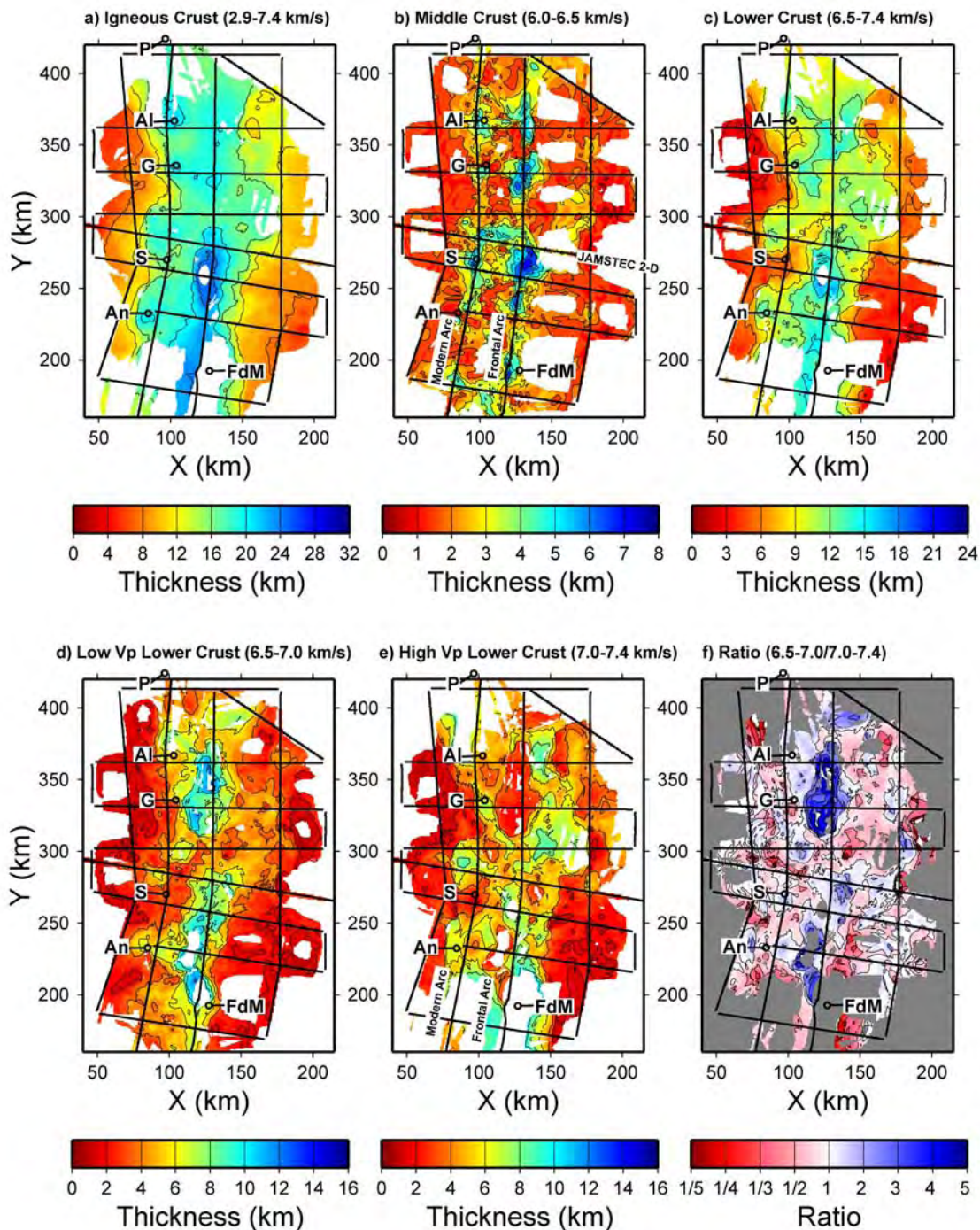


**Figure 11.** Isopachs calculated from 3-D velocity model for (a) igneous crust ( $2.9\text{--}7.4\text{ km s}^{-1}$ ), (b) middle crust ( $6.0\text{--}6.5\text{ km s}^{-1}$ ), (c) lower crust ( $6.5\text{--}7.4\text{ km s}^{-1}$ ), (d) low-velocity lower crust ( $6.5\text{--}7.0\text{ km s}^{-1}$ ), (e) high-velocity lower crust ( $7.0\text{--}7.4\text{ km s}^{-1}$ ), and (f) ratio of low-velocity lower crust to high-velocity lower crust. The thickness of the lower-crustal layers is only shown where ray coverage exists at both the upper and lower isovelocity contours. Note that the color scale for the isopach thicknesses varies between different parts of this figure. P, Al, G, S, and An are the active volcanic islands of Pagan, Alamagan, Guguan, Sarigan, and Anatahan, respectively. FdM is Ferdinand de Medinilla on the frontal arc.

which are constrained primarily by first arrivals from the JAMSTEC survey, are present at a depth of 22 km beneath the modern arc. The inference of a  $P$  wave velocity of  $8.0\text{ km s}^{-1}$  from an approximately east–west oriented

profile in the same location that a north–south profile of the 3-D survey indicates a velocity of approximately  $7.6\text{ km s}^{-1}$  may imply 5% azimuthal anisotropy in the upper mantle beneath this part of the modern arc, with the fast direction

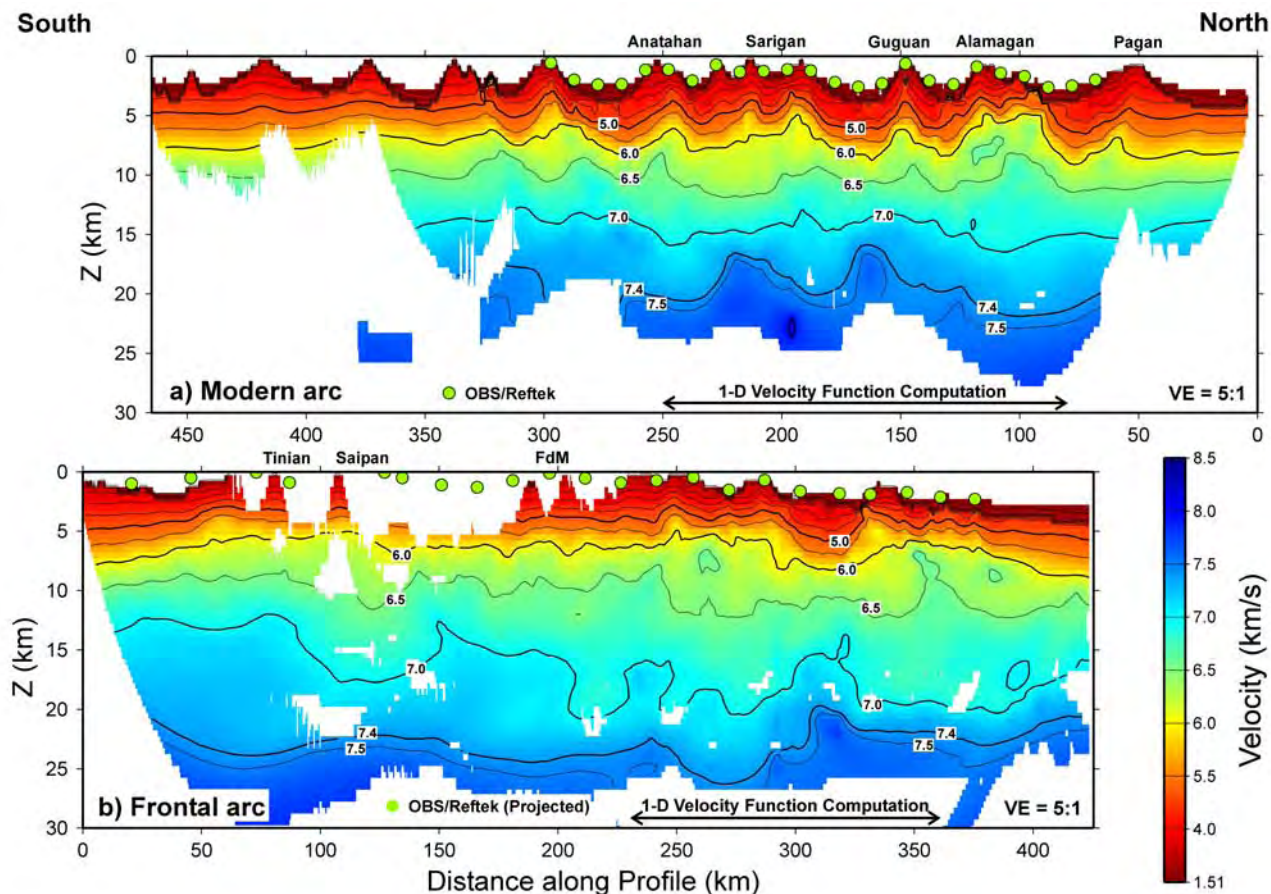


**Figure 12.** Vertical slices extracted from 3-D velocity model showing (a) along modern arc and (b) along frontal arc. The two sections are aligned such that a given latitude corresponds approximately to a vertical line through the two sections. The locations of OBS and Reftek receivers are shown by the solid green circles. The section along the frontal arc does not correspond exactly to shot line 20/21 (see Figure 2) because it was extracted from the region to the west where ray density in the middle and lower crust is greatest; receiver locations are projected onto the section from the east. Vertical exaggeration is 5:1.

parallel to the direction of back-arc spreading, as is typically expected in oceanic crust [Francis, 1969]. However, the inclusion of wide-angle reflections in the analysis of the JAMSTEC 2-D line [Takahashi *et al.*, 2007] produces lower velocities in this part of the upper mantle and implies a relatively small discrepancy. In summary, the 3-D seismic survey is consistent with the earlier inference of  $P$  wave velocities immediately beneath the Moho that are lower than the global average of  $8.1 \text{ km s}^{-1}$  [Takahashi *et al.*, 2007].

#### 5.4. Along-Arc Velocity Sections

[30] To compare the structures of the modern and frontal arcs, we have extracted from the 3-D velocity model a vertical section along shot line 10 and another section close to line 20/21 (Figure 12); the location of the latter was chosen to intersect the highest density of rays in the middle and lower crust (Figure 6), but this section still samples the axis of the frontal arc because shot points of line 20/21 were east of Saipan (Figure 2). In general, the best-constrained parts of the displayed sections correspond to the regions beneath the OBS arrays, and we restrict our observations to these areas.

[31] The volcanic edifices and the intervening accumulations of sediment are well represented in the section along the modern arc (Figure 12a). The high gradient zone across which velocities increase with depth to  $3.0\text{--}4.0 \text{ km s}^{-1}$  marks the basement interface. In the upper 4 km of the igneous crust the velocity gradient is approximately  $0.5 \text{ m s}^{-1}$ . Many of the velocity contours in the upper crust mimic the geometry of the seafloor, but above 15 km below sea level the undulations of the contours decrease with increasing depth down to about 15 km below sea level, resulting in the  $7.0 \text{ km s}^{-1}$  contour being subhorizontal below the modern arc. We have quantified these observations by calculating correlation coefficients of individual contours with the seafloor within a 30-km-wide swath centered on line 10. Correlation coefficients decrease from 0.95 for the  $2000 \text{ m s}^{-1}$  contour to 0.45 for the  $5000 \text{ m s}^{-1}$  contour, and the  $7000 \text{ m s}^{-1}$  contour has a negative coefficient of  $-0.27$ . The deeper contours exhibit much greater relief. For example, the  $7.4 \text{ km s}^{-1}$  isovelocity contour that we consider to represent the Moho varies between 16 km and 22 km below sea level but has a low negative correlation of  $-0.18$  with the seafloor.

[32] Beneath the Eocene frontal arc the velocity gradient in the upper igneous crust is generally similar to that of the modern arc (Figure 12b), and the velocity contours also mimic the bathymetry, which is more subdued than along the modern arc. Within a 30-km-wide swath around line 20/21, correlation coefficients vary from 0.97 for the 2000  $\text{m s}^{-1}$  contour to 0.68 for the 5000  $\text{m s}^{-1}$  contour. In contrast to the modern arc, however, the deeper velocity contours, for example, 7000  $\text{m s}^{-1}$ , under the frontal arc appear to become more rugose with increasing depth, suggesting a higher degree of heterogeneity within the lower crust above a Moho that varies between 20 km and 26 km below sea level. The northward shoaling of the Moho is associated with an increase in seafloor depth, and more generally beneath the frontal arc the 7400  $\text{m s}^{-1}$  isovelocity contour has a negative correlation coefficient with the seafloor of  $-0.55$ . Although this coefficient is not particularly high, it does indicate that a crustal root related to the volcanic seafloor topography may be more likely under the longer-lived Eocene frontal arc than the modern arc.

## 6. Discussion

[33] The 3-D  $P$  wave velocity model derived by tomographic inversion of first arrivals reveals a dramatic lateral variability at all levels of the crust that appears, with some exceptions, to be correlated with the location of past and present volcanism (Figures 2, 9, and 11). This variability is very evident along the strike of the arc, not only along the modern arc, in which isolated volcanoes have not yet linked to form a continuous structure after only 3–4 Ma of evolution, but also along the frontal arc, in which 35 Ma of activity might be expected to have created a relatively uniform average structure. This significant variability, by a factor of 2 in the thickness of specific velocity ranges (Figures 11b and 11c) that are widely used in petrological models and growth rate calculations [e.g., *Holbrook et al.*, 1999; *Takahashi et al.*, 2007], provides a caveat to most published arc evolution models that are based on single arc-perpendicular transects; such single profiles may be unrepresentative of the average arc.

[34] To capture the first-order properties of the crust along the modern arc and the Eocene frontal arc, we have computed representative 1-D velocity-depth functions where they are best constrained within the primary 3-D survey grid. These 1-D velocity functions have been estimated by averaging along strike the vertical sections displayed in Figure 12 where ray coverage exists and is deepest, that is, 80 km to 250 km along the profile in Figure 12a and 230 km to 360 km in Figure 12b. The two functions demonstrate the main differences between the modern volcanic arc and the Eocene frontal arc: For a given depth over a range of 3–6 km below sea level,  $P$  wave velocities are 240–360  $\text{m s}^{-1}$  lower in the upper crust of the modern arc; at a depth of 15 km below sea level, which corresponds to the lower crust, velocities are 280  $\text{m s}^{-1}$  higher beneath the modern arc (Figure 13).

[35] The  $P$  wave velocities of igneous crustal rocks decrease with increasing temperature [*Birch*, 1943; *Kern*, 1978; *Christensen*, 1979], and in the absence of melting a reduction in lower-crustal velocity of 0.12  $\text{km s}^{-1}$  has been suggested for the Aleutian arc relative to the same depth in

the fore-arc region [*Fliedner and Klemperer*, 1999]. The thermal structure of the Mariana arc is not well known, but a similar difference in velocities is predicted at a depth of 20 km if the geothermal gradient varies from a high value of 40°C  $\text{km}^{-1}$  in the active arc to 25°C  $\text{km}^{-1}$  in the fore arc. Depth slices through our 3-D velocity model show no indication of a  $P$  wave velocity reduction in the middle or lower crust under the modern volcanoes, most of which are characterized by higher velocity. Temperature clearly cannot explain the elevated lower-crustal velocities beneath the modern active arc, which is likely to be hotter than the frontal arc. Temperature may contribute to the reduced upper crustal velocities along the modern arc, but at depths less than 7 km the predicted variation due to temperature is small, probably less than 0.04  $\text{km s}^{-1}$ , and much less than the observed difference. Accumulations of partial melt may be significant locally, but if so, their dimensions must be considerably less than the 20 km resolution of the tomographic inversion.

[36] Given the relatively small effect of temperature on the magnitude of seismic velocity variation at a given depth, we interpret the velocity variations inferred in the upper crust in terms of porosity, and we interpret the variations in the middle and lower crust in terms of mineral composition related to the volcanic arc's magmatic evolution. We constrain this interpretation with laboratory measurements of seismic velocity on arc rocks exhumed from the middle and upper crust in the Izu collision zone that have been published previously by *Kitamura et al.* [2003].

### 6.1. Tanzawa Plutonic Complex

[37] A suite of Miocene tonalitic and gabbroic plutons from the middle crust of the northern Izu-Bonin arc, known as the Tanzawa plutonic complex (Figure 1), was exhumed in the collision with the Honshu arc that began approximately 6 Ma ago [*Nitsuma*, 1989; *Kawate and Arima*, 1998]. These plutons, which have K-Ar ages of 7 Ma [*Saito et al.*, 1991], intruded volcanic rocks, hemipelagic sediments, and volcanoclastic sediments of the Miocene (17–11 Ma) Tanzawa Group whose metamorphism indicates a maximum depth of approximately 6 km [*Arai*, 1987]. Following their correction to a common temperature of 25°C and also to confining pressure from depth, tomographic velocities estimated in the Mariana arc crust can be compared to laboratory  $P$  wave velocity measurements on a representative set of samples from the Tanzawa plutonic complex [*Kitamura et al.*, 2003]. The 1-D velocity functions derived for the Mariana modern and frontal arcs were corrected using a geothermal gradient of 25°C  $\text{km}^{-1}$ , which is an average value for island arcs [*Furukawa*, 1993], and a thermal coefficient of  $-0.04 \text{ m s}^{-1} \text{ } ^\circ\text{C}^{-1}$  (solid lines in Figure 13). For the samples from the Tanzawa plutonic complex, *Kitamura et al.* [2003] found very little variation of seismic velocity with temperature up to 400°C and estimated thermal coefficients between  $-0.027 \text{ m s}^{-1} \text{ } ^\circ\text{C}^{-1}$  and  $0.053 \text{ m s}^{-1} \text{ } ^\circ\text{C}^{-1}$ . If we had used a coefficient of  $-0.4 \text{ m s}^{-1} \text{ } ^\circ\text{C}^{-1}$  based on a broad range of crustal rocks [*Rudnick and Fountain*, 1995], the corrected tomographic velocities would be  $\sim 0.2 \text{ km s}^{-1}$  larger at a depth of 20 km (dashed lines in Figure 13). The reason for the low variation of velocity with temperature of the Tanzawa samples relative to most crustal rocks is not clear, but it may be

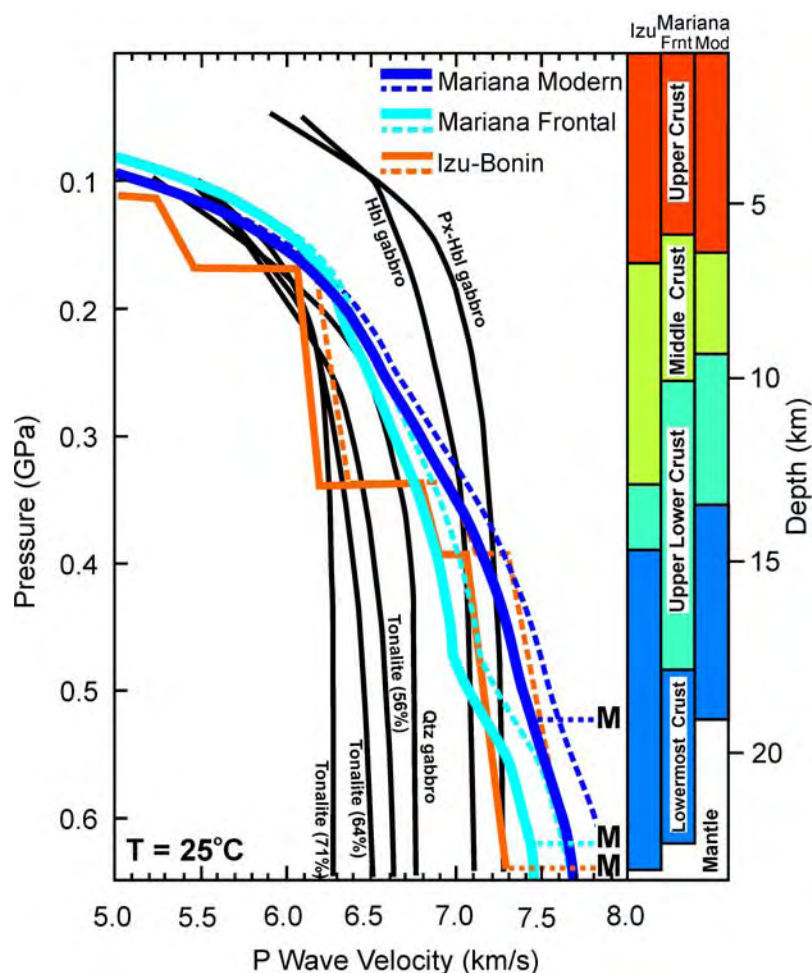


**Figure 13.** Comparison of laboratory measurements of  $P$  wave velocity on tonalitic and gabbroic rocks from the Tanzawa plutonic complex (after Kitamura *et al.* [2003]) with averaged 1-D seismic velocity functions from the Mariana arc (Figure 12). The 1-D velocity functions from the northern Izu-Bonin arc [Takahashi *et al.*, 1998] are also shown. The seismic velocity-depth functions have been converted to velocity-pressure and corrected to a temperature of  $25^{\circ}\text{C}$  (see text). The solid lines correspond to correction with a temperature coefficient of  $-0.04 \text{ m s}^{-1} \text{ }^{\circ}\text{C}^{-1}$ , which is a representative value for measurements made on samples from the Tanzawa plutonic complex [Kitamura *et al.*, 2003]. The dashed lines correspond to correction with a coefficient of  $-0.4 \text{ m s}^{-1} \text{ }^{\circ}\text{C}^{-1}$ , which is an average value for crustal rocks [Rudnick and Fountain, 1995]. The thicknesses of the different crustal layers, which have been defined by the in situ velocities in the seismic models, are also indicated. The tonalite samples are identified by their  $\text{SiO}_2$  content. Qtz, quartz; Px, pyroxene; Hbl, hornblende. M indicates the inferred location of the Moho.

attributable to a combination of a limited range of temperature measurements and nonlinear behavior above  $300\text{--}600^{\circ}\text{C}$  [Kitamura *et al.*, 2003; Kern and Richter, 1981]. Our velocity functions were converted from depth to lithostatic pressure using an empirical relation between velocity and density [Brocher, 2005].

[38] The laboratory  $P$  wave velocities of the Tanzawa tonalitic rocks all exhibit a velocity of  $6.2 \text{ km s}^{-1}$  at  $0.23 \text{ GPa}$ , and there is little to distinguish between them at midcrustal depths ( $\sim 8\text{--}12 \text{ km}$ ). The velocities of these tonalite samples correlate well with velocity profiles estimated for the middle crust of the northern Izu arc [Takahashi *et al.*, 1998] (Figure 13), but their velocities are as much as  $0.35 \text{ km s}^{-1}$  lower than the values we have

inferred in the Mariana arc at similar depths using 3-D seismic tomography. (The characteristics of the different seismic velocity models will be discussed in section 7.) The velocities of the gabbro samples, which originated in the middle to upper crust, vary more widely than the tonalites. Although the hornblende gabbro and pyroxene-hornblende gabbro have velocities that are  $0.35\text{--}0.55 \text{ km s}^{-1}$  greater than the Mariana velocity functions at  $0.25 \text{ GPa}$ , the quartz gabbro, with a velocity of  $6.45 \text{ km s}^{-1}$ , matches the Mariana velocity functions well both at this confining pressure and throughout the middle crust.

[39] At a confining pressure of  $0.35 \text{ GPa}$ , which corresponds to the upper part of the lower crust ( $\sim 13 \text{ km}$  depth), temperature-corrected  $P$  wave velocities in the Mariana arc

are greater than  $6.7 \text{ km s}^{-1}$ . At this pressure the velocities of all the tonalite samples are below  $6.5 \text{ km s}^{-1}$ , indicating that tonalite is unlikely to make up a large proportion of the lower crust. Within the lower crust of both the modern and Eocene Mariana arcs, the increase in velocity with depth is well represented by a downward transition from silica-rich gabbroic rocks to pyroxene-hornblende gabbro. The significant difference between these two velocity functions (active arc and frontal arc) arises from the much greater thickness of the shallower, lower-velocity lower crust beneath the remnant frontal arc, which is consistent with a composition between quartz gabbro and hornblende gabbro. Temperature-corrected  $P$  wave velocities greater than approximately  $7.3 \text{ km s}^{-1}$  are likely to indicate rocks such as norite, troctolite, or orthopyroxenite characteristic of pyroxene restites [Kitamura *et al.*, 2003]. In our 3-D tomographic velocity model the thickness of the region with velocities between  $7.3 \text{ km s}^{-1}$  and  $7.7 \text{ km s}^{-1}$  is not well constrained because any sharp transition to mantle rocks may have been smoothed vertically over a few kilometers, but our tomographic velocity functions are consistent with the existence of such rocks immediately above the seismic Moho.

## 6.2. Arc Structure

### 6.2.1. Upper Crust

[40] Upper crustal  $P$  wave velocities as low as  $3\text{--}4 \text{ km s}^{-1}$  are required just below the basement interface to fit first arrivals at small offsets. Velocities as low as  $2.5\text{--}3.0 \text{ km s}^{-1}$  have been inferred in the extrusive basaltic layer of  $0\text{--}3 \text{ Ma}$  old oceanic crust using OBS surveys, and a gradual increase in velocity to  $3.5\text{--}4.5 \text{ km s}^{-1}$  by  $4\text{--}5 \text{ Ma}$  and to  $4.0\text{--}5.5 \text{ km s}^{-1}$  at ages greater than  $50 \text{ Ma}$  has been documented [White, 1984]. In young oceanic crust the upper part of the igneous crust typically comprises pillow basalts, talus, and perhaps interlayered sediments that result in a high average porosity, and this porosity is largely responsible for the low  $P$  wave velocities. The effects of hydrothermal circulation lead to the filling of voids, a reduction in porosity, and an increase in the seismic velocity of the upper crust with age. The factors that control the seismic velocities of the upper igneous crust of an oceanic volcanic arc are similar to those that play a role in the development of oceanic crust; for example, subaqueous eruption of pillow basalts and mass-wasting from steep volcanic slopes are common. The low  $P$  wave velocities in the shallowmost igneous crust of the modern arc are likely due to high porosity within the volcanic layer. The higher upper crustal velocities of the older frontal arc probably reflect a reduction of porosity with age similar to that seen in normal oceanic crust. Since tonalitic rocks from the Tanzawa plutonic complex exhibit velocities between  $5.5 \text{ km s}^{-1}$  and  $6.0 \text{ km s}^{-1}$  at pressures less than  $0.2 \text{ GPa}$ , we suggest that the deeper upper crust of the Mariana arc may comprise substantial volumes of volcanic rocks subsequently intruded by plutons of tonalitic and perhaps quartz gabbroic composition.

### 6.2.2. Middle Crust

[41] In our 3-D velocity model, which lacks intracrustal discontinuities, we have defined the midcrust to be the region with in situ velocities between  $6.0 \text{ km s}^{-1}$  and  $6.5 \text{ km s}^{-1}$ . These velocities are too low to correspond to most gabbroic rocks, with the exception of quartz gabbro, but the Mariana velocity functions are also up to  $0.3 \text{ km s}^{-1}$

higher than the velocities of the Tanzawa tonalites at similar depths. We consider this midcrust to be on average of “intermediate” composition; however, it is likely an oversimplification to associate a single lithology with this region of our velocity model. Mapping of the Tanzawa plutonic complex suggests that the middle to upper crust of the Izu arc includes plutonic rocks that range from pyroxene-hornblende gabbro to relatively quartz-rich tonalite, with the tonalitic rocks being the later intrusions [Kawate and Arima, 1998]. We therefore suggest that the midcrust we have identified in the Mariana arc comprises tonalitic and gabbroic rocks with a range of compositions similar to the Tanzawa complex but that on average the composition of this region is similar to quartz gabbro, that is, andesitic.

[42] With velocities of  $6.1\text{--}6.3 \text{ km s}^{-1}$  the  $4\text{--}7\text{-km}$ -thick midcrustal layer of the Izu-Bonin arc (along profile a in Figure 1) has been interpreted to be tonalite produced by intracrustal differentiation of an initially basaltic crust [Suyehiro *et al.*, 1996; Takahashi *et al.*, 1998; Taira *et al.*, 1998]. A recent 2-D seismic survey along this arc (profile b in Figure 1) has revealed a  $6.0\text{--}6.5 \text{ km s}^{-1}$  midcrustal layer that varies in thickness between  $2 \text{ km}$  and  $8 \text{ km}$  [Kodaira *et al.*, 2007]. Our Mariana 3-D survey shows that the  $6.0\text{--}6.5 \text{ km s}^{-1}$  midcrustal region thins to  $2 \text{ km}$  between the active volcanoes of the modern Mariana arc. Although the 3-D survey indicates a more laterally extensive,  $3\text{--}6\text{-km}$ -thick midcrust beneath the older frontal arc, in general, the middle crust between the Mariana fore-arc and back-arc regions is less than  $3 \text{ km}$  thick, which is significantly less than the average thickness inferred in the northern Izu-Bonin arc.

### 6.2.3. Lower Crust

[43] The  $6.5\text{--}7.4 \text{ km s}^{-1}$  range of in situ velocity that we have chosen to represent the Mariana lower crust is similar to the  $P$  wave velocities of  $6.8\text{--}7.3 \text{ km s}^{-1}$  and  $6.6\text{--}7.4 \text{ km s}^{-1}$  that have been used previously to define the lower crust of the Izu-Bonin [Suyehiro *et al.*, 1996] and Mariana arcs, respectively [Takahashi *et al.*, 2007]; the  $6.5 \text{ km s}^{-1}$  isovelocity contour corresponds closely to the base of the middle crust (Figure 10). In the case of the  $35\text{-km}$ -thick Aleutian oceanic arc, velocities of  $6.5\text{--}7.4 \text{ km s}^{-1}$  define the midcrust, but this region is underlain by rocks with velocities of  $7.3\text{--}7.7 \text{ km s}^{-1}$  [Shillington *et al.*, 2004], which would lie largely beneath the Moho of our 3-D model.

[44] The thickness of the upper part of the Mariana lower crust with velocities between  $6.5 \text{ km s}^{-1}$  and  $7.0 \text{ km s}^{-1}$  characterizes the difference between the modern and frontal arcs. The globally averaged velocity of oceanic lower crust is  $6.95 \text{ km s}^{-1}$  [White *et al.*, 1992], and the velocities of gabbroic rocks recovered from ocean crust by drilling are  $6.5\text{--}7.4 \text{ km s}^{-1}$  [Iturrino *et al.*, 1991, 1996].  $P$  wave velocities below  $6.9 \text{ km s}^{-1}$  are difficult to simulate in pristine gabbros using models of mantle melting and may be best explained in oceanic crust by fracture porosity arising from ridge-crest faulting and thermal contraction [Korenaga *et al.*, 2002]. Although thermal contraction and faulting associated, for example, with arc rifting may serve to reduce the velocity of gabbroic rocks within the Mariana arc, it is also possible that velocities of  $6.5\text{--}6.9 \text{ km s}^{-1}$  indicate a region comprising both gabbroic and intermediate composition plutons that give the region its quartz gabbro bulk composition. The rugose velocity contours in the vertical

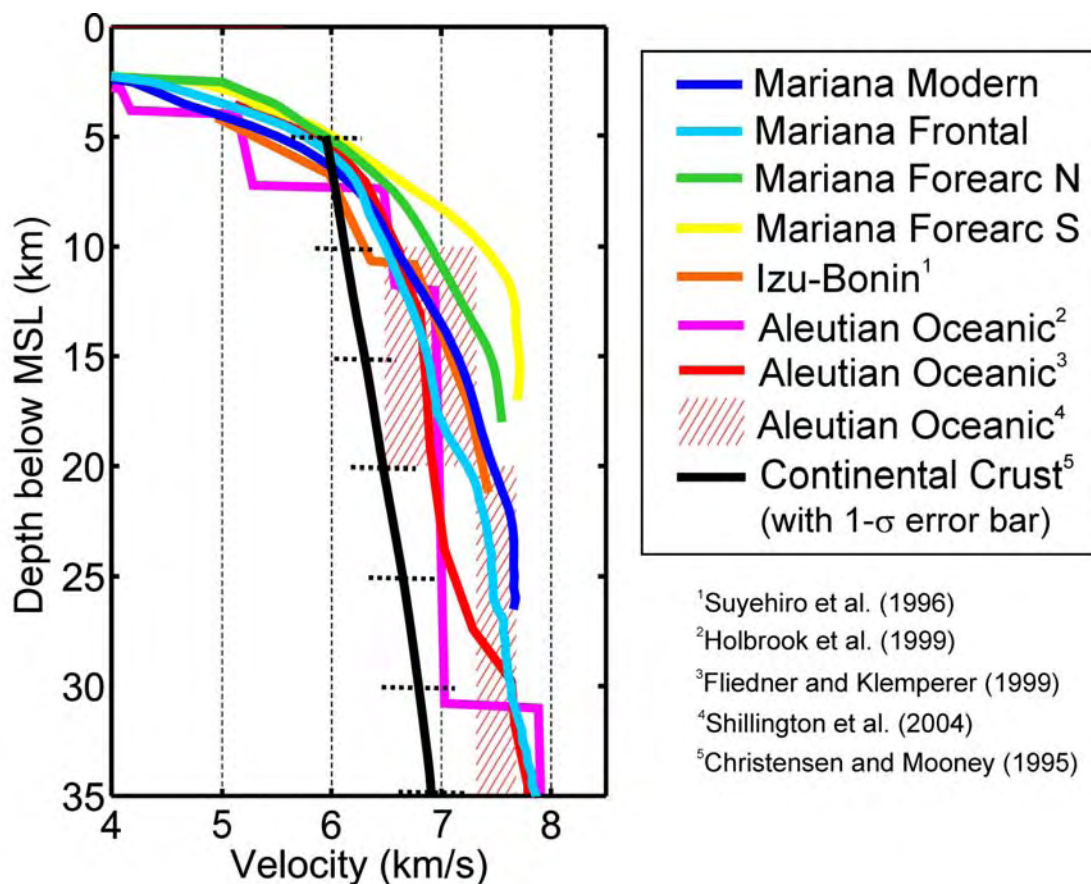


**Figure 14.** Comparison of average 1-D velocity functions from the Mariana, Izu-Bonin, and Aleutian oceanic island arcs. Upper crustal  $P$  wave velocities are  $240\text{--}360\text{ m s}^{-1}$  less beneath the modern Mariana arc than under the Eocene frontal arc, likely because of greater fracturing and porosity within the modern volcanic edifices. In contrast, the lower crust of the modern arc at 15 km depth has velocities that are  $280\text{ m s}^{-1}$  higher than beneath the frontal arc. (With the Moho inferred to be as shallow as 16 km below sea level beneath the modern arc, average velocities corresponding to depths greater than 15 km may not be indicative of the lower crust.) The velocity variation of the modern Mariana arc appears to be most similar to the results obtained from the active Izu-Bonin arc farther north, but both velocity functions from Mariana arc crust indicate that the crust here is significantly more mafic than typical continental areas. MSL indicates mean sea level.

section along the frontal arc (Figure 12b) are likely an indication of this heterogeneity. Along the Izu arc a 2–8-km-thick layer with velocities between  $6.5\text{ km s}^{-1}$  and  $6.8\text{ km s}^{-1}$  is interpreted to comprise intermediate composition plutons [Kodaira *et al.*, 2007]. As in the Tanzawa plutonic complex rocks with both andesitic and basaltic composition are found in the exhumed midcrust of the Kohistan arc in Pakistan, where the original crustal thickness is estimated to be approximately 40 km [Miller and Christensen, 1994]; at in situ temperature and pressure, predicted velocities for these rocks are  $6.5\text{--}7.5\text{ km s}^{-1}$  [Shillington *et al.*, 2004].

[45] Theoretical calculations [Korenaga *et al.*, 2002] and compilations of  $P$  wave velocities from rock samples [Christensen and Mooney, 1995; Kitamura *et al.*, 2003] corresponding to 10–20 km depth imply that in situ velocities of  $7.0\text{--}7.4\text{ km s}^{-1}$  in the Mariana lower crust represent quartz-poor gabbroic plutons. Temperature correction of in situ velocities using a thermal coefficient of  $-0.4\text{ m s}^{-1}\text{ }^{\circ}\text{C}^{-1}$  results in the highest velocity functions

shown in Figure 13 (dashed lines) and implies a velocity of approximately  $7.5\text{ km s}^{-1}$  immediately above the Moho; these velocities would be consistent with mafic/ultramafic cumulates in the deepest part of the lower crust.

#### 6.2.4. Uppermost Mantle

[46] Moho reflections are intermittently observed in the 3-D seismic data set beneath the Mariana arc (e.g., Figure 3a), demonstrating the widespread existence of this interface, in general agreement with the more finely sampled 2-D survey of Takahashi *et al.* [2007]. Below the deepest inferred crust of the modern arc the 1-D velocity function indicates  $7.7\text{ km s}^{-1}$  at a depth of 23–27 km, while velocities under the frontal arc are approximately  $7.6\text{--}7.7\text{ km s}^{-1}$  at 27–30 km (Figure 14). Although constrained by only a small number of raypaths, these velocities are similar to those of the lower crust beneath the Aleutian oceanic arc, which were interpreted to represent mafic-ultramafic cumulates or garnet granulites [Shillington *et al.*, 2004]. Using petrologic modeling of results from their 2-D survey, Takahashi *et al.* [2007] have suggested that the region immediately below the Mariana

arc may also be mafic-ultramafic cumulates; our inferred velocities are consistent with their hypothesis. Although velocities of  $7.7 \text{ km s}^{-1}$  are commonly observed in the upper mantle of fore-arc regions, where serpentinization of peridotites is postulated [Hyndman and Peacock, 2003], this seems unlikely beneath the active and frontal arcs where high temperatures associated with active magmatism should act to dehydrate serpentine. The preliminary results of a passive seismic tomography survey of the Mariana arc show that velocities of  $7.7 \text{ km s}^{-1}$  extend to depths as great as 100 km below the arc [Barklage et al., 2006]. At such depths, which are well below the petrologic Moho, high temperatures are the most plausible explanation for  $P$  wave velocities below  $8.0 \text{ km s}^{-1}$ , and such thermal effects may be responsible for the low velocities we infer immediately below the seismic Moho.

### 6.3. Evolution of Mariana Arc Crust

[47] Rocks with velocities of  $7.0\text{--}7.4 \text{ km s}^{-1}$  make up the greatest proportion of the lower crust along the modern arc, which has a relatively short ( $<4 \text{ Ma}$ ) magmatic history. The limited development of middle crust here implies that a period of  $>4 \text{ Ma}$  is necessary to generate significant volumes of intermediate composition crust. Thus if magmatism ceases after a relatively short period, the crust formed will have a largely mafic composition, and we suggest that the 15-km-thick fore-arc crust just east of the frontal arc ( $280 < y < 340$ ) represents a short-lived episode of magmatism that occurred early in the evolution of the Mariana arc system [Stern and Bloomer, 1992]. Along the modern arc the circular shapes of the middle and lower-crustal isopach contours (Figure 11c) suggest that large-scale magmatic activity here has been focused on a few centers, but the minimum crustal thickness of 13 km, which is at least double the thickness of the original oceanic crust, indicates that the crust has also thickened at distances of up to 20 km from the intrusive centers.

[48] Beneath the frontal arc the isopach contours are somewhat wider and subparallel to strike, suggesting that a number of magmatic centers have merged over the longer history of this region. Relative to the modern arc the decreased  $P$  wave velocities in the lower crust of the Mariana frontal arc appear to be due to a thickened upper region, that is, the interval between the  $6.5 \text{ km s}^{-1}$  and  $7.0 \text{ km s}^{-1}$  isovelocity contours (Figure 12). Along the frontal arc, thicker regions of this low-velocity lower crust ( $190 < y < 280$  and  $320 < y < 380$  in Figure 11d) lie below the thickest midcrust ( $180 < y < 220$ ,  $240 < y < 280$ , and  $320 < y < 380$  in Figure 11b), indicating that the growth of these two crustal levels is probably related. We have proposed that arc crust with velocities of  $6.5\text{--}7.0 \text{ km s}^{-1}$ , which are at the low end of the range of values typically associated with gabbroic rocks, comprises a mixture of gabbroic and intermediate intrusions. We suggest that the growth of the middle crust and immediately underlying, low-velocity lower crust is a function of age and is a result of a  $>40 \text{ Ma}$  history during which repeated episodes of magmatic intrusion into the lower crust have resulted in anatexis and intracrustal differentiation. Intermediate composition magmas generated by this process rose to form the midcrust along the volcanic centers, but we suggest that

some of these magmas solidified in the immediately underlying lower crust, creating a region with seismic properties similar to quartz gabbro.

[49] Along the frontal arc the thickest regions of low-velocity ( $6.5\text{--}7.0 \text{ km s}^{-1}$ ) lower crust appear to occur above thinner regions of high-velocity ( $7.0\text{--}7.4 \text{ km s}^{-1}$ ) lower crust ( $190 < y < 250$  and  $320 < y < 370$  in Figure 11e). Generation of intermediate composition magma by melting of basaltic crust will produce a residuum of pyroxenite restite [Nakajima and Arima, 1998], implying an increase in the volume of high-velocity mafic rocks in the lower crust. Two alternative explanations for the observed decrease in the thickness of the high-velocity lower crust beneath regions of growth in the low-velocity lower crust are as follows:

[50] 1. With  $P$  wave velocity of  $7.4\text{--}7.7 \text{ km s}^{-1}$  [Christensen and Mooney, 1995], pyroxenite restite will lie below the  $7.4 \text{ km s}^{-1}$  velocity contour we have identified as the Moho, suggesting that the generation of intermediate composition melts can raise the level of this velocity contour in the petrologic lower crust and produce the apparent thinning of high-velocity lower crust we interpret. The observed along-strike variations in thickness of the high-velocity lower crust would then imply that intracrustal differentiation is not a uniform process and is segmented along the arc.

[51] 2. With a density of  $3.2\text{--}3.9 \text{ g cm}^{-3}$  [Nakajima and Arima, 1998], which is similar to or greater than peridotite in the uppermost mantle, restite may have detached from the arc crust and foundered [Behn and Kelemen, 2006]. If this speculation is correct, then arc crust with a relatively thin high-velocity lower crust, that is, the high-ratio regions in Figure 11f, would be an indication that this delamination process has occurred.

[52] Although lower-crustal velocities are less beneath the Mariana frontal arc than below the modern arc, these velocities still fall outside the range of values normally associated with continental crust of normal thickness, implying that the Mariana arc has a relatively mafic lower-crustal composition (Figure 14). The longer history of the frontal arc, which was subject to rifting during both the Eocene and Miocene [Crawford et al., 1981], would have allowed a longer period for crustal differentiation following arc initiation, permitting the development of a less mafic middle and lower crust. Such a process would reduce the seismic velocities, but in the Mariana arc this process did not produce a significant crustal thickness with velocities less than  $6.5 \text{ km s}^{-1}$  that would be a clear characteristic of continental crust. In contrast, Kodaira et al. [2007] has identified four 20–40 km sections along the Izu arc to the north where seismic velocities are similar to those of continental crust. We speculate that the difference in crustal composition between the Izu arc and Mariana frontal arc may be related to differences in the magmatic supply, which was ultimately terminated in the Mariana arc by Miocene rifting that displaced the frontal arc from its position over the rising mantle melts.

## 7. Petrologic Modeling

[53] Simplified modeling of arc growth provides a way to estimate the relative proportions of the different petrologic components of the crust. Following the approach of

**Table 1.** Comparison of Seismologically Measured Lower-Crustal Volume With Petrologic Estimates

Layer Volumes, per Unit Arc Length	Mariana 2-D Survey, <sup>a</sup> km <sup>-2</sup>	Mariana 3-D Survey, <sup>b</sup> km <sup>-2</sup>
	<i>Seismic Estimates</i>	
Sediments $1.5 < V < 2.9$ km s <sup>-1</sup>	311	176 (-0/+0)
Upper crust $2.9 < V < 6.0$ km s <sup>-1</sup>	588	646 (+9/-9)
Middle crust $6.0 < V < 6.5$ km s <sup>-1</sup>	591	369 (-3/-3)
Lower crust $6.5 < V < 7.4$ km s <sup>-1</sup>	1349	1376 (+210/-47)
	<i>Petrologic Calculation From Observed Upper and Middle Crust</i>	
Estimated restite	1098-1773	685 (-5/-5)-1106 (-8/-9)
Estimated cumulates	642-833	479 (+0/-5)-598 (-1/-6)
Estimated lower crust	1740-2606	1164 (-5/-10)-1704 (-9/-14)
	<i>Deviation From Seismologically Inferred Crust, %</i>	
Lower crust	+29-+93	-15 (-12/+3)-+24 (-17/+4)

<sup>a</sup>From *Takahashi et al.* [2007].

<sup>b</sup>Limiting velocity is  $V_M = 8.0$  (-0.2/+0.2).

*Takahashi et al.* [2007], an initial crust can be considered to form from the differentiation of a primary basaltic magma. The differentiation of basaltic magma that later rises from the mantle wedge creates additional cumulates plus melts that rise through the original crust to solidify and form the present-day upper crust. During this process the initial hydrated crust, with the exception of the cumulates, partially melts to create a midcrustal region considered to be tonalitic in composition, leaving a layer of restite [*Tatsumi*, 2000]. Using a cumulate fraction of 22% [e.g., *Ghiorso and Sack*, 1995] and assuming a range of 25–35% partial melting [*Beard and Lofgren*, 1991], *Takahashi et al.* [2007] calculated the volumes of restite and cumulates that form the petrologic lower crust of the Mariana arc from the upper and middle crust defined seismologically by their 2-D survey and showed that the volume of the petrologic lower crust required to generate the middle crust is 1.3–1.9 times the volume of the seismologically defined lower crust. From this result they argue that the low sub-Moho velocities beneath the arc represent ultramafic cumulates, that is, petrologic lower crust, providing a possible explanation for the velocity of 7.7 km s<sup>-1</sup>.

[54] The upper and middle crust vary significantly in thickness along the strike of the Mariana arc, and the 3-D velocity model we have derived should provide a more reliable estimate of the volumes of the respective crustal regions. We have calculated the volumes of sedimentary rocks, upper crust, middle crust, shallow lower crust, and deep lower crust from the 3-D velocity model between a line 70 km west of shot line 10 and a line 70 km east of line 20/21 (Figure 2) using the following velocity ranges, respectively: 1.51–2.9 km s<sup>-1</sup>, 2.9–6.0 km s<sup>-1</sup>, 6.0–6.5 km s<sup>-1</sup>, 6.5–7.0 km s<sup>-1</sup>, and 7.0–7.4 km s<sup>-1</sup>; the total volume of lower crust is obtained by summing the last two regions (Table 1). To assess the reliability of these volume estimates, we repeated this calculation twice using 3-D tomographic velocity models derived with identical parameters from two alternative initial velocity models in which the limiting upper mantle velocity,  $V_M$ , was 7.8 km s<sup>-1</sup> and 8.2 km s<sup>-1</sup>, resulting in a 0.1 km s<sup>-1</sup> difference from the preferred starting model at 6.35 km below sea level. The RMS traveltimes misfits of these two initial models, which are 0.473 s and 0.512 s, respectively, contrast with the lower value of 0.420 s of the preferred starting model. With the

exception of the deeper lower crust the crustal volume estimates do not vary greatly with the choice of starting model, indicating that most of the crust is well constrained under the assumption of this type of initial model and small along-strike variation in regions of limited or no ray coverage. For example, in the upper crust at 5 km below sea level, ray coverage is limited to the vicinity of the airgun lines (Figure 9), but we assume that the smoothness constraints imposed on the velocity model by the tomographic inversion result in realistic values for the upper crustal velocities between the airgun lines. However, the estimated volume of lower crust with velocities of 7.0–7.4 km s<sup>-1</sup> increases as the mantle velocity of the initial model is lowered, demonstrating that the volume of this deeper region is subject to a greater degree of uncertainty, as noted previously.

[55] Since the middle crust thins along strike away from the volcanic edifices, our estimate of the proportion of middle crust is less (14%) than that derived from the 2-D seismic survey (21%). Our calculated proportion of middle crust does not vary significantly with the part of the arc selected; for example, two different estimates made using 40-km-wide regions centered on shot line 10 along the modern arc and line 20/21 along the frontal arc are both 14%. Using these 3-D volume estimates and the method of *Takahashi et al.* [2007], we have calculated the volume of petrologic lower crust required to produce the observed thickness of tonalitic middle crust and find that the petrologic estimate is consistent with the seismological estimate derived using the preferred and the two bounding starting models (+28/-27%, Table 1). So the seismic Moho could be at the base of the petrologic crust. This 3-D result contrasts with the 2-D seismic survey, which indicated that a significant volume of petrologic lower crust lies below the Moho. Although our best estimates of the volumes of crust from the 3-D velocity model suggest that the petrologic and seismological Moho may coincide, we next show that the greater uncertainties associated with the compositional interpretation of velocities in the middle crust are sufficient to leave open the possibility of a petrologic crust-mantle boundary deeper than the Moho.

[56] If our low-velocity lower crust contains a significant volume of rocks of intermediate composition, then the volume of petrologic lower crust required to generate all rocks of intermediate composition (middle crust and intermediate portion of the “low-velocity lower crust”) will

exceed the lower-crustal volume derived from our 3-D seismic survey. If rocks of intermediate composition make up 25% of our low-velocity, lower-crustal layer, then a result similar to that of *Takahashi et al.* [2007] is obtained. Alternatively, changing our definition of “middle crust” to include  $P$  wave velocities up to  $6.6 \text{ km s}^{-1}$  (instead of  $6.5 \text{ km s}^{-1}$ , as we prefer), a velocity which corresponds to the value for low-silica tonalites at this depth [*Kitamura et al.*, 2003], will increase the volume of the middle crust by 28% and also result in a mismatch of the seismological and petrologic estimates of lower-crustal volume. These uncertainties imply that petrologic modeling based on the seismic velocities alone is insufficient to distinguish whether the sub-Moho region in our 3-D model represents ultramafic cumulates or whether the Moho and the crust-mantle boundary coincide.

[57] Estimates of the volume of the middle crust from modeling of both refractions and reflections can be significantly greater than those from first-arrival inversions because of the introduction of a laterally continuous interface at the base of the middle crust to explain intracrustal reflections [*Suyehiro et al.*, 1996; *Takahashi et al.*, 2007] (e.g., Figure 10). Such reflections, however, are not widely evident in the Mariana 3-D data set, and we suggest that the intermediate middle crust that has been identified by others as a precursor to continental crust may in reality be laterally variable, even intermittent, and forms only a small proportion of the total crust.

## 8. Rates of Arc Growth

[58] The 3-D wide-angle seismic survey of the Mariana ocean island arc reveals significant variations in seismic velocity and crustal thickness along strike that are impossible to resolve with a single 2-D survey. Using an estimate derived from the volume of the model with  $P$  wave velocities less than  $7.4 \text{ km s}^{-1}$  (a proxy for the Moho) in a 20-km-wide corridor along strike, the average crustal thickness of the 3–4 Ma old active arc is 18 km. The crust of the Eocene frontal arc is, on average, 21 km thick. However, along strike the crust of the modern arc varies in thickness between 13 km and 22 km, while the Eocene arc varies between 18 km and 24 km. Although the older part of the Mariana arc has a thicker crust, the relationship between age and crustal thickness is clearly not linear. The two episodes of arc rifting, which created the Palau-Kyushu Ridge and West Mariana Ridge, separated substantial volumes of crust from the present-day arc, making it difficult to estimate a magma production rate over its approximately 45 Ma history. Assuming that the Palau-Kyushu Ridge has a similar crustal volume to the  $2057 \text{ km}^3 \text{ km}^{-1}$  of the West Mariana Ridge [*Takahashi et al.*, 2007] and combining these volumes with our estimate for the Mariana arc of  $2566 \text{ km}^3 \text{ km}^{-1}$ , which is the sum of the crustal components listed in Table 1, yields a magmatic production rate of  $80 \text{ km}^3 \text{ km}^{-1} \text{ Ma}^{-1}$  if the original oceanic crust were 6 km thick. This average rate is similar to the value of  $82 \text{ km}^3 \text{ km}^{-1} \text{ Ma}^{-1}$  obtained for the Aleutian ocean arc [*Holbrook et al.*, 1999] and the range of  $30\text{--}85 \text{ km}^3 \text{ km}^{-1} \text{ Ma}^{-1}$  estimated for several oceanic arcs in the western Pacific [*Dimalanta et al.*, 2002] but considerably greater than the growth rate of Phanerozoic continental crust of  $20\text{--}40 \text{ km}^3$

$\text{km}^{-1} \text{ Ma}^{-1}$  [*Reymer and Schubert*, 1984]. Studies of tephra from the Mariana arc suggest three periods of increased volcanic activity at 35–24 Ma, 18–11 Ma, and 6–0 Ma that may correlate with periods of more rapid arc growth [*Lee et al.*, 1995]. Consequently, the 18 km crustal thickness of the <4 Ma old modern arc may be the result of an above-average magmatic production rate. Under the assumption that a 40-km-wide east–west corridor centered on shot line 10 had not been significantly affected by earlier arc magmatism, this crustal production rate is estimated to be  $116 \text{ km}^3 \text{ km}^{-1} \text{ Ma}^{-1}$ .

## 9. Crustal Tomography of Island Arcs

[59] Our 3-D tomographic inversion of first arrivals was constrained to produce a smooth final velocity model that represents the volumetric distribution of  $P$  wave velocity in the subsurface.  $PmP$  arrivals are sometimes observed beneath the arc, but intracrustal reflections are less evident. These observations are likely a result of both the variability in the lateral continuity of the reflectors and the difficulty in identifying reflections amongst a variety of other phases such as first-arrival reverberations and refracted diffractions associated with the complex seafloor topography. Our use of the 3-D FAST tomography code [*Zelt and Barton*, 1998] did not allow us to include wide-angle reflections in the inversion. Wide-angle reflections have the potential to constrain short-wavelength structures such as the Moho more accurately than methods based on first arrivals alone (e.g., Figure 10). *Kodaira et al.* [2007] demonstrated the lack of continuity of several wide-angle reflectors recorded by a 2-D survey of the northern Izu-Bonin arc by depth migrating the traveltimes picks. In a heterogeneous region such as the Mariana arc the common algorithmic requirement that a reflecting interface be continuous across a 3-D model may not be justified, and the best approach to inclusion of 3-D wide-angle reflections may be in the form of “floating reflectors.” In 2-D marine wide-angle surveys, such as the JAMSTEC line, which often have receivers deployed every 5–10 km, it is easier to identify  $PmP$  and intracrustal reflections than in a more sparse 3-D survey. However, inclusion of these data in a traveltimes inversion requires the 2-D assumption of in-plane reflection in addition to the key requirement of reflector continuity.

[60] In future 3-D surveys of oceanic arcs the offset of shot and receiver lines from extreme topography such as the volcanoes would permit the recording of a simpler seismic wavefield with fewer shadow zones, less traveltimes variability, and fewer interfering coherent arrivals (compare Figure 3a with Figure 3c), while still allowing the reconstruction of the volumetric seismic velocity variation under the volcanic centers. The resulting easier identification of secondary arrivals will then allow a more objective assessment of the distribution of reflecting interfaces beneath the arc. In addition, interpretation of the amplitude variation of various crustal phases will be facilitated if the focusing and defocusing effects of the seafloor topography are avoided, or at least minimized.

## 10. Conclusions

[61] The 3-D subsurface  $P$  wave velocity distribution along 220 km of the Mariana island arc has been obtained

by tomographic inversion of first-arrival traveltimes from a wide-angle seismic survey comprising orthogonal shot and receiver lines. The thickest igneous crust, averaging 21 km, is located beneath the remnant frontal arc that dates from the Eocene. The modern arc averages 18 km in thickness with the Moho deepest beneath the volcanoes of Anatahan, Sarigan, and Alamagan. Although the middle crust, which is defined by velocities of 6.0–6.5 km s<sup>-1</sup>, reaches a thickness of 6 km along the older frontal arc, this region has a thickness of only 3 km when averaged across the modern and frontal arcs. Comparison of the inferred average seismic velocity functions with velocity measurements on samples of exhumed arc crust suggests the presence of tonalitic rocks in the transition from upper to middle crust. Seismic velocities in the middle crust and the immediately underlying lower crust, which is characterized by velocities between 6.5 km s<sup>-1</sup> and 7.0 km s<sup>-1</sup>, are consistent with a bulk composition similar to quartz gabbro that may be explained by a mixture of gabbroic and more intermediate intrusions. Consequently, at a depth of 15 km, velocities in the lower crust are 280 m s<sup>-1</sup> slower under the frontal arc than under the modern arc. The greater thickness of the middle and shallower lower crust beneath the frontal arc is attributed to intracrustal differentiation that has occurred since the Eocene. The increase of lower-crustal velocity with depth is consistent with a gradual transition from a quartz gabbro composition to pyroxene-hornblende gabbro. Lower crust under the modern arc, the northern fore arc, and perhaps the frontal arc south of the 3-D survey grid is characterized by a greater thickness with velocities above 7.0 km s<sup>-1</sup>, consistent with limited intracrustal differentiation. The growth of the modern arc at a rate which may be as high as 116 km<sup>3</sup> km<sup>-1</sup> Ma<sup>-1</sup> over the last 4 Ma indicates a significant level of temporal variability in the arc's evolution.

[62] Although the 3-D seismic survey provides evidence of a reduction in the mafic character of Mariana arc crust over time, seismic velocities in the middle and lower crust imply a primarily basaltic composition that differs from the more andesitic sections of the northern Izu-Bonin arc. Furthermore, the average seismic velocity structure of the Mariana arc is generally similar to that of the Aleutian oceanic arc above 25 km depth.

[63] **Acknowledgments.** We thank the captain and crew of the R/V *Ewing* and the OBSIP technical staff for their expert assistance during the acquisition of the field data. IRIS Data Management Center provided copies of the field data tapes. Andrew Goodliffe provided the integrated 3-D bathymetric data that was used to define the seafloor in the tomographic inversion. Roland Günther calculated the locations of the OBS on the seafloor using the direct water wave arrival times. Colin Zelt provided some helpful insights into the operation of the FAST tomography code. Comments from Bob Stern and Derek Thorkelson plus thoughtful reviews by Steve Holbrook, Tom Brocher, and associate editor Clifford Thurber improved the final manuscript. This project was funded by NSF OCE-MARGINS grant 00-01956 to SLK, NSERC Discovery grant 155519 to AJC, and through a Stanford University Blaustein Visiting Fellowship to AJC while at Stanford University.

## References

- Arai, T. (1987), Tectonics of Tanzawa mountains: Constraints from metamorphic petrology, *J. Geol. Soc. Jpn.*, *93*, 185–200.
- Arculus, R. J. (1981), Island arc magmatism in relation to the evolution of the crust and mantle, *Tectonophysics*, *75*, 113–133.
- Barklage, M. E., J. Conder, D. Wiens, P. Shore, H. Shiobara, H. Sugioka, and H. Zhang (2006), 3-D seismic tomography of the Mariana mantle wedge from 2003–2004 passive component of the Mariana subduction factory imaging experiment, *Eos Trans. AGU*, *87*(52), Fall Meet. Suppl., Abstract T23C-0506.
- Beard, J. S., and G. E. Lofgren (1991), Dehydration melting and water-saturated melting of basaltic and andesitic greenstones and amphibolites, *J. Petrol.*, *32*, 365–401.
- Behn, M. D., and P. B. Kelemen (2006), Stability of arc lower crust: Insights from the Talkeetna arc section, south-central Alaska, and the seismic structure of modern arcs, *J. Geophys. Res.*, *111*, B11207, doi:10.1029/2006JB004327.
- Behn, M. D., G. Hirth, and P. B. Kelemen (2007), Trench-parallel anisotropy produced by foundering of arc lower crust, *Science*, *317*, 108–111.
- Bibee, L. D., G. G. Shor Jr., and R. S. Lu (1980), Inter-arc spreading in the Mariana Trough, *Mar. Geol.*, *35*, 183–197.
- Birch, F. (1943), Elasticity of igneous rocks at high temperatures and pressures, *Geol. Soc. Am. Bull.*, *54*, 263–286.
- Bloomer, S. H., and J. W. Hawkins (1987), Petrology and geochemistry of boninite series volcanic rocks from the Mariana Trench, *Contrib. Mineral. Petrol.*, *97*, 361–377.
- Brocher, T. M. (2005), Empirical relations between elastic wavespeeds and density in the Earth's crust, *Bull. Seismol. Soc. Am.*, *95*, 2081–2092.
- Card, K. D. (1990), A review of the Superior Province of the Canadian Shield, a product of Archean accretion, *Precambrian Res.*, *48*, 99–156.
- Christensen, N. I. (1979), Compressional wave velocities in rocks at high temperatures and pressures, critical thermal gradients, and crustal low velocity zones, *J. Geophys. Res.*, *84*, 6849–6857.
- Christensen, N. I., and W. D. Mooney (1995), Seismic velocity structure and composition of the continental crust, *J. Geophys. Res.*, *100*, 9761–9788.
- Clift, P., and P. Vannucchi (2004), Controls on tectonic accretion versus erosion in subduction zones: Implications for the origin and recycling of the continental crust, *Rev. Geophys.*, *42*, RG2001, doi:10.1029/2003RG000127.
- Crawford, A. J., L. Beccaluva, and G. Serri (1981), Tectono-magmatic evolution of the West Philippine-Mariana region and the origin of boninites, *Earth Planet. Sci. Lett.*, *54*, 346–356.
- Crawford, W. C., J. A. Hidebrand, L. M. Dorman, S. C. Webb, and D. A. Wiens (2003), Tonga Ridge and Lau Basin crustal structure from seismic refraction data, *J. Geophys. Res.*, *108*(B4), 2195, doi:10.1029/2001JB001435.
- De Bari, S. M., B. Taylor, K. Spencer, and K. Fujioka (1999), A trapped Philippine Sea plate origin for MORB from the inner slope of the Izu-Bonin trench, *Earth Planet. Sci. Lett.*, *174*, 183–197.
- Dimalanta, C., A. Taira, G. P. Yumul Jr., H. Tokuyama, and K. Mochizuki (2002), New rates of western Pacific island arc magmatism from seismic and gravity data, *Earth Planet. Sci. Lett.*, *202*, 105–115.
- Fliedner, M. M., and S. L. Klemperer (1999), Structure of an island-arc: Wide-angle seismic studies in the eastern Aleutian Islands, Alaska, *J. Geophys. Res.*, *104*, 10,667–10,694.
- Fliedner, M. M., and S. L. Klemperer (2000), Crustal structure transition from oceanic arc to continental arc, eastern Aleutian Islands and Alaska Peninsula, *Earth Planet. Sci. Lett.*, *179*, 567–579.
- Francis, T. J. G. (1969), Generation of seismic anisotropy in the upper mantle along the mid-oceanic ridges, *Nature*, *221*, 162–165.
- Fryer, P. (1995), Geology of the Mariana Trough, in *Backarc Basins: Tectonics and Magmatism*, edited by B. Taylor, pp. 237–279, Plenum, New York.
- Furukawa, Y. (1993), Magmatic processes under arc and formation of the volcanic front, *J. Geophys. Res.*, *98*, 8309–8319.
- Ghiorso, M. S., and R. O. Sack (1995), Chemical mass-transfer in magmatic processes IV. A revised and internally consistent thermodynamic model for the interpolation and extrapolation of liquid-solid equilibria in magmatic systems at elevated temperatures and pressures, *Contrib. Mineral. Petrol.*, *119*, 197–212.
- Grow, J. A. (1973), Crustal and upper mantle structure of the central Aleutian arc, *Geol. Soc. Am. Bull.*, *84*, 2169–2192.
- Günther, R. H., S. L. Klemperer, and A. M. Goodliffe (2006), Modeling sideswipe in 2D oceanic seismic surveys from sonar data: Application to the Mariana arc, *Tectonophysics*, *420*, 333–343.
- Hamilton, W. B. (1981), Crustal evolution by arc magmatism, *Philos. Trans. R. Soc. London, Ser. A*, *301*, 279–291.
- Hickey, R. L., and F. A. Frey (1982), Geochemical characteristics of boninite series volcanics: Implications for their source, *Geochim. Cosmochim. Acta*, *45*, 2099–2115.
- Hickey-Vargas, R. L., and M. Reagan (1987), Temporal variations of isotope and rare earth element abundances from Guam: Implications for the evolution of the Mariana Island arc, *Contrib. Mineral. Petrol.*, *97*, 497–508.
- Holbrook, W. S., D. Lizaralde, S. McGeary, N. Bangs, and J. Diebold (1999), Structure and composition of the Aleutian Island arc and implication for continental crustal growth, *Geology*, *27*, 31–34.

- Hussong, D. M., and S. Uyeda (1981), Tectonic processes and the history of the Mariana arc, a synthesis of the results of Deep Sea Drilling Project Leg 60, *Initial Rep. Deep Sea Drill. Proj.*, 60, 909–929.
- Hyndman, R. D., and S. M. Peacock (2003), Serpentinization of the forearc mantle, *Earth Planet. Sci. Lett.*, 212, 417–432.
- Iturrino, G. J., N. I. Christensen, S. Kirby, and M. H. Salisbury (1991), Seismic velocities and elastic properties of oceanic gabbroic rocks from Hole 735B, *Proc. Ocean Drill. Program Sci. Results*, 118, 227–244.
- Iturrino, G. J., D. J. Miller, and N. I. Christensen (1996), Velocity behavior of lower crustal and upper mantle rocks from a fast-spreading ridge at Hess Deep, *Proc. Ocean Drill. Program Sci. Results*, 147, 417–440.
- Johnson, L. E., P. Fryer, B. Taylor, M. Silk, D. L. Jones, W. V. Sliter, T. Itaya, and T. Ishii (1991), New evidence for crustal accretion in the outer Mariana forearc: Cretaceous radiolarian cherts and MORB-like lavas, *Geology*, 19, 811–814.
- Kawate, S., and M. Arima (1998), Petrogenesis of the Tanzawa plutonic complex, central Japan: Exposed felsic crust of the Izu-Bonin-Mariana arc, *Isl. Arc*, 7, 342–358.
- Kay, R. W., and S. M. Kay (1993), Delamination and delamination magmatism, *Tectonophysics*, 219, 177–189.
- Kern, H. (1978), The effect of high temperature and high confining pressure on compressional wave velocities in quartz-bearing and quartz-free igneous and metamorphic rocks, *Tectonophysics*, 44, 185–203.
- Kern, H., and A. Richter (1981), Temperature derivatives of compressional and shear wave velocities in crustal and mantle rocks at 6 kbar confining pressure, *J. Geophys.*, 49, 47–56.
- Kitamura, K., M. Ishikawa, and M. Arima (2003), Petrological model of the northern Izu-Bonin-Mariana arc crust: Constraints from high pressure measurements of elastic wave velocities of the Tanzawa plutonic rocks, central Japan, *Tectonophysics*, 371, 213–221.
- Kobayashi, K., S. Kasuga, and K. Okino (1995), Shikoku basin and its margins, in *Backarc Basins: Tectonics and Magmatism*, edited by B. Taylor, pp. 381–405, Plenum, New York.
- Kodaira, S., T. Sato, N. Takahashi, A. Ito, Y. Tamura, Y. Tatsumi, and Y. Kaneda (2007), Seismological evidence for variable growth of arc crust along the Izu intraoceanic arc, *J. Geophys. Res.*, 112, B05104, doi:10.1029/2006JB004593.
- Korenaga, J., P. B. Kelemen, and W. S. Holbrook (2002), Methods for resolving the origin of large igneous provinces from crustal seismology, *J. Geophys. Res.*, 107(B9), 2178, doi:10.1029/2001JB001030.
- Leat, P. T., and R. D. Larter (2003), Intra-oceanic subduction systems: Introduction, in *Intra-Oceanic Subduction Systems: Tectonic and Magmatic Processes*, edited by P. T. Leat and R. D. Larter, *Geol. Soc. Spec. Publ., London*, 219, 1–17.
- Lee, J., R. J. Stern, and S. H. Bloomer (1995), Forty million years of magnetic evolution in the Mariana arc: The tephra glass record, *J. Geophys. Res.*, 100, 17,671–17,687.
- Lizarralde, D., W. S. Holbrook, S. McGeary, N. Bangs, and J. Diebold (2002), Crustal construction of a volcanic arc, wide-angle results from the western Alaska Peninsula, *J. Geophys. Res.*, 107(B8), 2164, doi:10.1029/2001JB000230.
- Meijer, A. (1983), Pb and Sr isotopic data bearing on the origin of volcanic rocks from the Mariana arc system, *Geol. Soc. Am. Bull.*, 87, 1358–1369.
- Miller, D. J., and N. I. Christensen (1994), Seismic signature and geochemistry of an island arc: A multidisciplinary study of the Kohistan accreted terrane, northern Pakistan, *J. Geophys. Res.*, 99, 11,623–11,642.
- Murauchi, S. (1972), Crustal structure of the Japan Sea, *Kagaku*, 42, 367–375.
- Nakajima, K., and M. Arima (1998), Melting experiments on hydrous low-K tholeiite: Implications for the genesis of tonalitic crust in the Izu-Bonin-Mariana arc, *Isl. Arc*, 7, 359–373.
- Nitsuma, N. (1989), Collision tectonics in the South Fossa Magna, Central Japan, *Mod. Geol.*, 14, 3–18.
- Okino, K., Y. Ohara, S. Kasuga, and Y. Kato (1999), The Philippine Sea: New survey results reveal the structure and the history of the marginal basins, *Geophys. Res. Lett.*, 26, 2287–2290.
- Pearce, J. A., S. R. van der Laan, R. J. Arculus, B. J. Murton, T. Ishii, J. A. Peate, and I. J. Parkinson (1992), Boninite and harzburgite from Leg 125 (Bonin-Mariana forearc): A case study of magma genesis during the initial stages of subduction, in *Proc. Ocean Drill. Program Sci. Results*, vol. 125, edited by L. H. Dearmont et al., pp. 623–659, Ocean Drill. Program, College Station, Tex.
- Ramachandran, K. (2001), Velocity structure of S. W. British Columbia and N. W. Washington from 3-D nonlinear seismic tomography, Ph.D. thesis, Univ. Victoria, Victoria, Canada.
- Ramachandran, K., S. E. Dosso, C. A. Zelt, G. D. Spence, R. D. Hyndman, and T. M. Brocher (2004), Upper crustal structure of southwestern British Columbia from the 1998 Seismic Hazards Investigation in Puget Sound, *J. Geophys. Res.*, 109, B09303, doi:10.1029/2003JB002826.
- Reagan, M. K., and A. Meijer (1984), Geology and geochemistry of early arc-volcanic rocks from Guam, *Geol. Soc. Am. Bull.*, 95, 701–713.
- Reymer, A., and G. Schubert (1984), Phanerozoic addition rates to the continental crust and crustal growth, *Tectonics*, 3, 63–77.
- Rudnick, L. R., and M. D. Fountain (1995), Nature and composition of the continental crust: A lower crustal perspective, *Rev. Geophys.*, 33, 267–309.
- Saito, K., I. Otomo, and T. Takai (1991), K-Ar dating of the Tanzawa tonalitic body and some restrictions on the collision tectonics in South Fossa Magna, central Japan, *J. Geomagn. Geoelectr.*, 43, 921–935.
- Seno, T., S. Stein, and A. E. Gripp (1993), A model for the motion of the Philippine Sea plate consistent with NUVEL and geological data, *J. Geophys. Res.*, 98, 17,941–17,948.
- Shillington, D. J., H. J. A. van Avendonk, W. S. Holbrook, P. B. Kelemen, and M. J. Hombach (2004), Composition and structure of the central Aleutian island arc from arc-parallel wide-angle seismic data, *Geochem. Geophys. Geosyst.*, 5, Q10006, doi:10.1029/2004GC000715.
- Steinhart, J. S. (1967), Mohorovicic discontinuity, in *International Dictionary of Geophysics*, vol. 2, edited by K. Runcorn, pp. 991–994, Elsevier, New York.
- Stern, R. J., and S. H. Bloomer (1992), Subduction zone infancy: Examples from the Eocene Izu-Bonin-Mariana and Jurassic California arcs, *Geol. Soc. Am. Bull.*, 104, 1621–1636.
- Stern, R. J., M. J. Fouch, and S. L. Klemperer (2003), An overview of the Izu-Bonin-Mariana subduction factory, in *Inside the Subduction Factory*, *Geophys. Monogr. Ser.*, vol. 138, edited by J. Eiler, pp. 175–222, AGU, Washington, D. C.
- Suyehiro, K., N. Takahashi, Y. Ariei, Y. Yokoi, R. Hino, M. Shinohara, T. Kanazawa, N. Hirata, H. Tokuyama, and A. Taira (1996), Continental crust, crustal underplating, and low-Q upper mantle beneath an oceanic island arc, *Science*, 272, 390–392.
- Taira, A., S. Saito, K. Aoike, S. Morita, H. Tokuyama, K. Suyehiro, N. Takahashi, M. Shinohara, S. Kiyokawa, J. Naka, and A. Klaus (1998), Nature and growth rate of the Northern Izu-Bonin (Ogasawara) arc crust and their implications for continental crust formation, *Isl. Arc*, 7, 395–407.
- Takahashi, N., K. Suyehiro, and M. Shinohara (1998), Implications from the seismic crustal structure of the northern Izu-Bonin arc, *Isl. Arc*, 7, 383–394.
- Takahashi, N., S. Kodaira, A. Ito, H. Shinohara, H. Sugioka, B. Kerr, I. Vlad, S. Klemperer, Y. Kaneda, and K. Suyehiro (2003), Deep seismic profiling across the Mariana arc-backarc system, *Indep. Admin. Inst. Jpn. Agency Mar.-Earth Sci. Technol. Yokosuka Jpn.*, 23, 55–68.
- Takahashi, N., S. Kodaira, S. Klemperer, Y. Tatsumi, Y. Kaneda, and K. Suyehiro (2007), Crustal structure and evolution of the Mariana intra-oceanic island arc, *Geology*, 35, 203–206.
- Tatsumi, Y. (2000), Continental crust formation by crustal delamination in subduction zones and complementary accumulation of enriched mantle I component in the mantle, *Geochem. Geophys. Geosyst.*, 1(12), doi:10.1029/2000GC000094.
- Taylor, B. (1992), Rifting and volcano-tectonic evolution of the Izu-Bonin-Mariana arc, in *Proc. Ocean Drill. Program Sci. Results*, vol. 126, edited by E. Maddox, pp. 627–651, Ocean Drill. Program, College Station, Tex.
- Taylor, S. R., and S. M. McLennan (1995), The geochemical evolution of the continental crust, *Rev. Geophys.*, 33, 241–265.
- Uyeda, S., and H. Kanamori (1979), Back-arc opening and the mode of subduction, *J. Geophys. Res.*, 84, 47–56.
- van der Hilst, R., R. Engdahl, W. Spakman, and G. Nolet (1991), Tomographic imaging of subducted lithosphere below northwest Pacific island arcs, *Nature*, 353, 37–42.
- White, R. S. (1984), Atlantic oceanic crust: Seismic structure of a slow-spreading ridge, in *Ophiolites and Oceanic Lithosphere*, edited by I. G. Gass et al., *Geol. Soc. Spec. Publ., London*, 13, 101–111.
- White, R. S., D. MacKenzie, and R. K. O'Nions (1992), Oceanic crustal thickness from seismic measurements and rare earth element inversions, *J. Geophys. Res.*, 97, 19,683–19,715.
- Zelt, C. A. (1998), Lateral resolution from three-dimensional seismic refraction data, *Geophys. J. Int.*, 135, 1101–1112.
- Zelt, C. A., and P. J. Barton (1998), 3-D seismic refraction tomography: A comparison of two methods applied to data from the Faroes Basin, *Geophys. J. Int.*, 103, 7187–7210.

A. J. Calvert, Department of Earth Sciences, Simon Fraser University, 8888 University Drive, Burnaby, BC, Canada V5A 1S6. (acalvert@sfu.ca)

B. C. Kerr and S. L. Klemperer, Department of Geophysics, Stanford University, Stanford, CA 94305-2215, USA. (bckerr@stanford.edu; sklemp@stanford.edu)

N. Takahashi, Japan Agency for Marine-Earth Science and Technology, 3173-25, Showa-machi, Kanazawa-ku, Yokohama 236-0001, Japan. (narumi@jamstec.go.jp)